Research on Stroboscopic Mapping Modeling and Bifurcation Characteristics of Grid-Connected Inverter Considering PWM Saturation

Le Chen, *Student Member, IEEE*, Yingjie He, *Senior Member, IEEE*, Yixiao Zhu,
and Jinjun Liu, *Fellow, IEEE*

***Abstract*—For the grid-connected inverter system, the sustained constant-amplitude oscillations often occur. At this time, the grid-connected current undergoes oscillation, and the PWM process appears saturation nonlinearity (i.e., overmodulation). However, the existing modeling methods cannot accurately model this hard nonlinearity, thereby explaining the phenomenon of grid-connected current oscillation. In this article, the step function is used to accurately represent the PWM saturation nonlinearity, and the accurate stroboscopic mapping model of three-phase grid-connected inverter system is established, and it is strictly proved that in a fundamental period, although the switching state type, sequence, and working time are different in any switching period of different sectors, the expression of stroboscopic mapping model is same and unique. Based on the precise stroboscopic mapping model, the bifurcation characteristics of the system when PWM saturation occurs are analyzed using the bifurcation diagrams and the root locus of Jacobian matrix, the accurate bifurcation boundary is obtained, and revealing the essential reasons for grid-connected current oscillation and its relationship with PWM saturation. The correctness of the theoretical analysis is finally verified by simulation and experiment.**

***Index Terms*—Grid-connected inverter, pulse width modulation (PWM) saturation, step function, stroboscopic mapping model, super-critical Hopf bifurcation, sustained constant-amplitude oscillation.**

I. INTRODUCTION

WITH the transformation of energy production and consumption, the traditional power system that relies on fossil fuels is shifting towards new generation power systems based on power electronics with a high proportion of renewable energy [1], [2]. Among them, the grid-connected inverters, as effective interfaces between the renewable energy generation and the power grid, occupy a high proportion in the power electronic power system [3], [4]. However, in addition to the switching nonlinearity of the power stage itself in the grid-connected inverter system [5], [6], when the system experiences sustained constant-amplitude oscillations due to factors such as power grid strength [7], [8], control parameters [9], [10], and grid voltage swell [11], [12], PWM may become saturated. At the same time, the grid-connected current distortion is severe, which affects the safe and stable operation of the system. Therefore, it is essential to apply the accurate and effective modeling methods and analyzing tools to reveal the dynamic behaviors of the strongly nonlinear systems such as grid-connected inverters.

For the saturation nonlinearity, the commonly used modeling method of small-signal linearization is no longer applicable because of the nondifferentiable turning point of its input and output characteristics [13]. The existing solution is the harmonic linearization method based on describing function theory, where the PWM saturation characteristics are equivalent to a proportional link with variable gain [14], [15], [16]. In [14], the describing function method was used to linearize the PWM saturation in a single-phase LCL grid-connected inverter, and the system structure diagram of the entire closed-loop system was established. Then, the generalized Nyquist stability criterion was applied to analyze the impact of the PWM saturation on the instability behavior of grid-connected inverters under different grid strengths. In [15] and [16], the saturation gain of PWM was solved based on the theory of multiple input describing function and iterative methods, and the sequence impedance model of a three-phase grid-connected inverter was established. Then, the logarithmic frequency stability criterion based on impedance was used to predict the oscillation amplitude and frequency that may be generated under weak grids. From the above-mentioned research, it can be seen that using the describing function method to analyze the PWM saturation characteristics is actually harmonic linearization in the frequency domain. This processing method can only be compatible with the impedance model or transfer function model [17], ignoring the nonlinear switching process of the inverter itself, so it cannot analyze the nonlinear

Manuscript received 7 November 2023; revised 9 February 2024; accepted 30 March 2024. Date of publication 9 April 2024; date of current version 16 May 2024. This work was supported in part by the Qinchuangyuan "Scientist + Engineer" Team Construction Project of Shaanxi Province under Grant 2024QCY-KXJ-138, in part by the Natural Science Foundation of Shaanxi Province under Grant 2023-JC-YB-367, in part by "Chunhui Plan" Cooperative Research Project of the Education Ministry under Grant 202200765, and in part by the Aeronautical Science Foundation of China under Grant 20230040070017. Recommended for publication by Associate Editor D. Xu. *(Corresponding author: Yingjie He.)*

Le Chen, Yingjie He, and Jinjun Liu are with the School of Electrical Engineering, Xi'an Jiaotong University, Xi'an 710049, China (e-mail: lechen@stu.xjtu.edu.cn; yjhe@mail.xjtu.edu.cn; jjliu@mail.xjtu.edu.cn).

Yixiao Zhu was with the School of Electrical Engineering, Xi'an Jiaotong University, Xi'an 710049, China. He is now with the Monolithic Power Systems, Hangzhou 310000, China (e-mail: 17728179342@stu.xjtu.edu.cn).

Color versions of one or more figures in this article are available at https://doi.org/10.1109/TPEL.2024.3386608.

Digital Object Identifier 10.1109/TPEL.2024.3386608

dynamic behaviors of the switching time scale and predict accurate parameter boundaries. In addition, the application of the describing function also has certain restrictions, such as the linear part of the system should have good low-pass filtering performance, and the sinusoidal response of the nonlinear part should not contain constant components [18].

The stroboscopic mapping model is most suitable for studying and analyzing the switching nonlinearity in piecewise-smooth dynamical systems such as power electronic converters and has the analytical ability of multiple time scale dynamics behavior [19], [20]. Li et al. [21] established the stroboscopic mapping model for the voltage-mode controlled full-bridge inverter and verified by accurate numerical simulation that the system will produce the fast-scale period-doubling bifurcation and the slow-scale Hopf bifurcation under different filter cut-off frequencies. The fast-scale instability of a three-level T-type single-phase inverter feeding diode-bridge rectifier with inductive load was studied in [22], which revealed that the essential cause of instability is the occurrence of period-doubling bifurcation, and analyzed the key parameters affecting system stability. The above-mentioned research objects are all analog control systems, and the stroboscopic mapping model can also accurately model the digital control system [23], [24], [25]. Lei et al. [23] established the stroboscopic mapping model for the digitally controlled single-phase grid-connected inverter system considering control delay, and the system stability was judged by solving the eigenvalues of Jacobian matrix, and the stable boundary of the control parameters was solved when the Hopf bifurcation does not occur. A simplified stroboscopic mapping modeling method is proposed in [24], which introduces the principle of state space average into the traditional stroboscopic mapping modeling method, while ensuring accuracy, it significantly reduces the complexity of the traditional stroboscopic mapping modeling process, and still accurately models the control delays, accurately analyzing the slow-scale and fast-scale dynamics of the system. Lei et al. [25] established the stroboscopic mapping model for the three-phase digitally controlled passive inverter system and analyzed its local oscillation phenomenon of the system, the conditions for the system to generate local oscillation and the relationship between control parameters and local oscillation points were obtained. However, no detailed proof was provided on whether the stroboscopic mapping models for three-phase inverters in different sectors are consistent. In addition, the stroboscopic mapping models established in the above-mentioned research works did not take into account the PWM saturation nonlinearity, so the bifurcation characteristics of the system when PWM saturation occurs have not been clearly studied.

It can be seen from the above-mentioned research status that, compared to other modeling methods, the stroboscopic mapping model can accurately model the sampling/holding and control delay and switching nonlinearity in digitally controlled inverters. However, how to model the PWM saturation nonlinearity, and the bifurcation characteristics when PWM saturation occurs have not been clearly studied. In addition, for three-phase inverters operating in different sectors, the switching state type, sequence, and working time are not the same, it remains to be proven whether their stroboscopic mapping model is the same and unique. To solve these problems, this article takes the digitally controlled three-phase grid-connected inverter with symmetrical regular sampling as the research object, establishes its accurate stroboscopic mapping model considering one beat delay, and introduces step function to accurately express the PWM saturation nonlinearity, and strictly proves that in a fundamental period, although the switching state type, sequence, and working time are different in any switching period of different sectors, the expression of stroboscopic mapping model is same and unique. Based on the precise stroboscopic mapping model, the bifurcation characteristics of the system when PWM saturation occurs are analyzed using the bifurcation diagrams and the root locus of Jacobian matrix, and the bifurcation boundary is accurately predicted, revealing the essential reasons for grid-connected current oscillation and its relationship with PWM saturation.

The rest of this article is organized as follows. Section II introduces the structure of the digitally controlled grid-connected inverter system, and analyzes the PWM saturation nonlinearity through two cases. In Section III, the step function is introduced to accurately represent PWM saturation nonlinearity, and the accurate stroboscopic mapping model of the system is established. It is proved that the expression of the stroboscopic mapping model is the same and unique in different sectors within a fundamental period. In Section IV, the accuracy of the established stroboscopic mapping model is verified by numerical simulation. Then, the bifurcation characteristics of the system when PWM saturation occurs are analyzed using the bifurcation diagram method and the root locus of Jacobian matrix, and the boundary of bifurcation parameters are accurately obtained, revealing the essential reasons for grid-connected current oscillation and its relationship with PWM saturation. Section V verifies the correctness of the theoretical analysis by experiment. Finally, Section VI concludes this article.

II. SYSTEM DESCRIPTION AND PWM SATURATION NONLINEARITY

A. System Description

The digitally controlled grid-connected inverter system is shown in Fig. 1. Among them, S_1–S_6 is the power switch tube, U_{dc} is the dc-side voltage, L_{f} is the filter inductance, R_{f} is the equivalent series resistance, u_{ga}, u_{gb}, and u_{gc} are the three-phase grid voltage, i_{La}, i_{Lb}, and i_{Lc} are the three-phase grid-connected current, u_{m} (u_{ma}, u_{mb}, u_{mc}) are the three-phase modulation signal, u_{gd} and u_{gq} are the *d*/*q*-axis components of the grid voltage. Assuming that the three-phase filtering circuit, line resistance, and grid voltage are completely symmetrical, and the dc-side voltage is constant, without considering the equivalent internal impedance of the grid.

B. Analysis of PWM Saturation Nonlinearity

Here are two examples. In situations such as increasing controller parameters or grid voltage swell, the PWM may

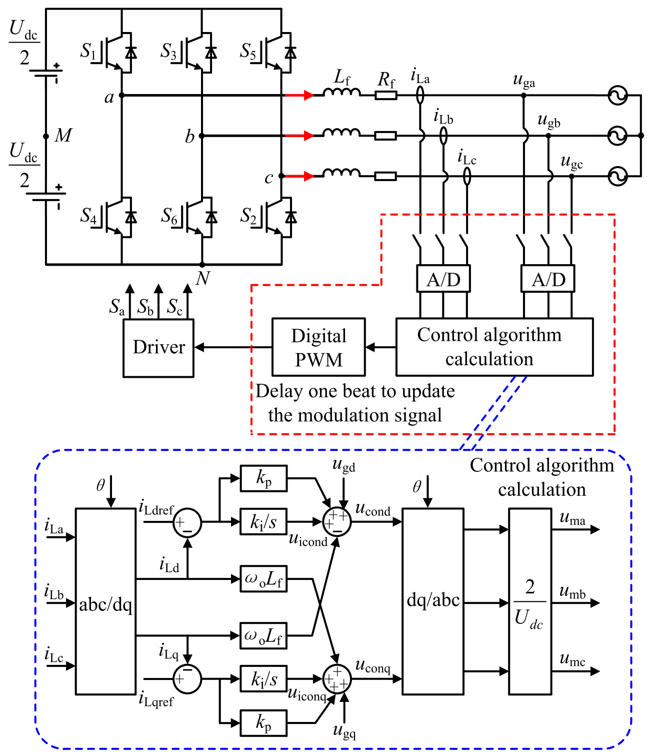

Fig. 1. Configuration of the three-phase grid-connected inverter system.

TABLE I
SYSTEM PARAMETERS

parameters	Value
DC-side voltage (U_{dc})	135 V
RMS of grid voltage (U_g)	40 V
filter inductance (L_f)	3.56 mH
Filter inductance resistance R_f	0.01 Ω
fundamental frequency (f_o)	50 Hz
switching frequency (f_s)	10 kHz
sampling frequency (f_{sa})	10 kHz
Controller proportional coefficient (k_p)	12
Controller integral coefficient (k_i)	2000
d-axis current controller reference value (i_{Ldref})	12 A
q-axis current controller reference value (i_{Lqref})	0 A

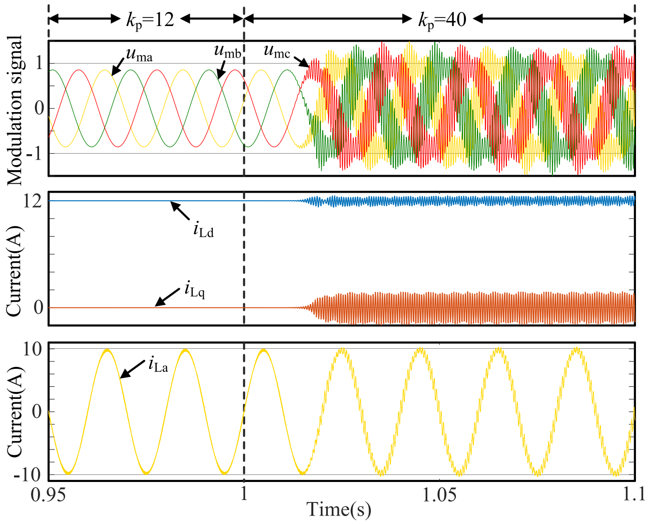

Fig. 2. Controller proportional coefficient k_p increases.

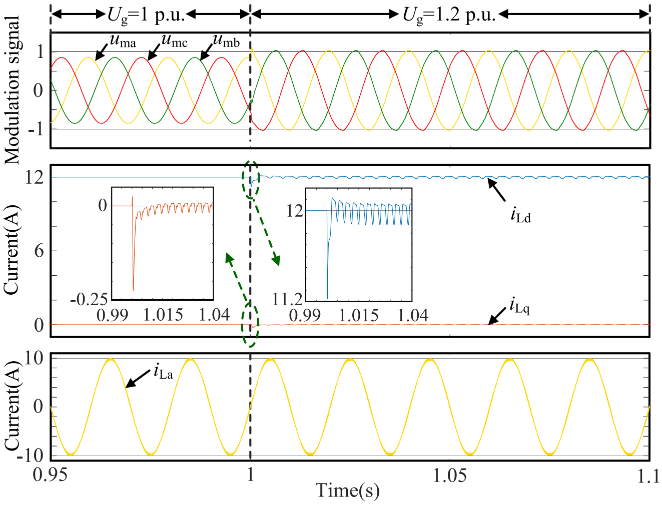

Fig. 3. Grid voltage swell.

experience saturation, which means that the three-phase modulation signal is overmodulation and the grid-connected current is distorted. The details are as follows. Simulating under the parameters given in Table I, Fig. 2 shows the overmodulation when the controller proportional coefficient k_p increases to 40 at $t = 1$ s, and Fig. 3 shows the overmodulation when the grid voltage abruptly swells to 1.2 p.u. at $t = 1$ s. It can be seen that the grid-connected current is distorted in both overmodulation cases, but there are differences between them. In Fig. 2, after k_p is changed, the *d/q*-axis component of grid-connected current i_{Ld}, i_{Lq} first oscillates and diverges, when PWM saturation occurs, i_{Ld} and i_{Lq} evolve into sustained constant-amplitude oscillations. In Fig. 3, after the grid voltage swells, PWM immediately saturates, and i_{Ld} and i_{Lq} first suddenly drop, then rise to near the reference value and continue to oscillate. In addition, in these two cases, the oscillation frequency of the grid-connected current is also different. Therefore, this article establishes an accurate stroboscopic mapping model considering PWM saturation, and then analyzes the essential reasons for the sustained oscillation of grid-connected current and its relationship with PWM saturation under these two conditions from the perspective of bifurcation.

For the overmodulation situation mentioned above, the PWM under saturated conditions can be equivalent as follows [26]. As shown in Fig. 4, taking the a-phase modulation signal u_{ma} as an example, when u_{ma} is greater than the carrier signal u_{cr} (but less than the carrier signal amplitude 1), the switch tube S_1 is turned ON. However, when the amplitude of u_{ma} is greater than 1, overmodulation will occur, and S_1 will continue to turn ON. As can be seen from the pulse waveform of S_1, it is consistent with the result obtained by comparing u_{ma} with the triangle carrier signal after "flattening" the part greater than 1 of u_{ma} (as shown by the red dashed line). It is like the modulation signal u_{ma} first passes through a saturation limiter and then is

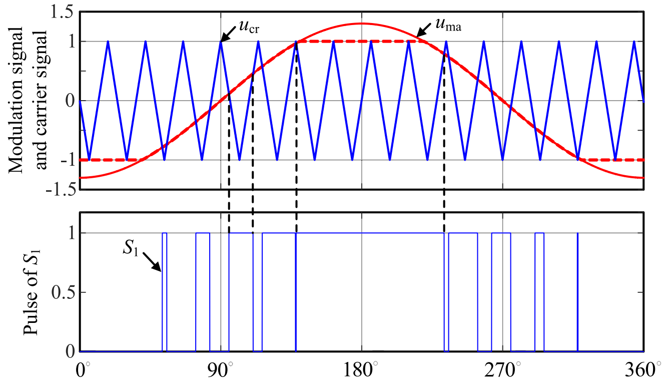

Fig. 4. PWM saturation (overmodulation).

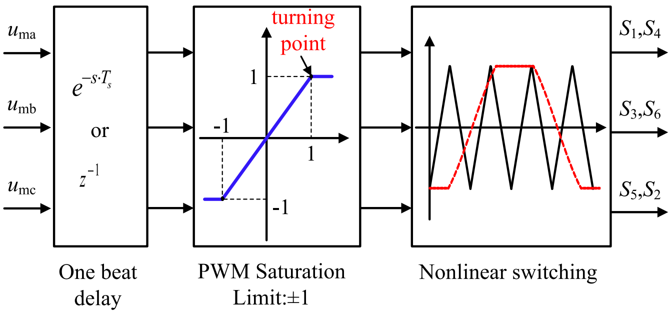

Fig. 5. Equivalent model of PWM under saturated conditions.

compared with the triangular carrier signal. Therefore, the PWM can be mathematically equivalent to three independent parts, as shown in Fig. 5. For one beat delay and nonlinear switching, the stroboscopic mapping model can accurately model them. However, for the PWM saturation limiting link, the widely used describing function method currently has certain restrictions and is not precise enough. The stroboscopic mapping model considering PWM saturation proposed in this article can accurately model the strong nonlinearity of PWM saturation. A detailed introduction is as follows.

III. STROBOSCOPIC MAPPING MODELING OF THREE-PHASE GRID-CONNECTED INVERTER SYSTEM

According to different sampling methods, discrete mapping is divided into stroboscopic mapping, synchronous switching mapping, and asynchronous switching mapping [27]. This article adopts the most commonly used stroboscopic mapping.

A. Switching Model

First, the switching model of the power stage is derived from the *abc*-frame. $S_{\rm i}$ (i = a, b, c) is defined as the switching function of the three-phase bridge arm, which can be expressed as

$$S_i(i=a,b,c) = \begin{cases} 1 \\ 0 \end{cases} \tag{1}$$

where $S_{\rm i} = 1$ indicates that the upper bridge arm of the *i*-phase is ON and the lower bridge arm is OFF. On the contrary, the upper bridge arm is OFF and the lower bridge arm is ON.

Since the above-mentioned assumptions are that the three-phase is completely symmetrical, combined with the KCL law, the following equation holds:

$$\begin{cases} u_{ga} + u_{gb} + u_{gc} = 0 \\ i_{La} + i_{Lb} + i_{Lc} \equiv 0 \end{cases}. \tag{2}$$

So the output voltage of the three-phase bridge arm can be represented by the switching function $S_{\rm i}$ (i = a, b, c) as follows:

$$\begin{cases} u_{ao} = \frac{U_{dc}}{3}(2S_a - S_b - S_c) \\ u_{bo} = \frac{U_{dc}}{3}(2S_b - S_a - S_c) \\ u_{co} = \frac{U_{dc}}{3}(2S_c - S_a - S_b) \end{cases}. \tag{3}$$

Write the KVL equations of the ac side of the inverter as

$$\begin{cases} L_f \frac{di_{La}}{dt} + R_f \cdot i_{La} = u_{ao} - u_{ga} \\ L_f \frac{di_{Lb}}{dt} + R_f \cdot i_{Lb} = u_{bo} - u_{gb} \\ L_f \frac{di_{Lc}}{dt} + R_f \cdot i_{Lc} = u_{co} - u_{gc} \end{cases}. \tag{4}$$

By substituting (3) into (4), the switching model of the power stage in the *abc*-frame can be obtained as

$$\frac{d}{dt}\begin{bmatrix} i_{La} \\ i_{Lb} \\ i_{Lc} \end{bmatrix} = -\frac{R_f}{L_f}\begin{bmatrix} i_{La} \\ i_{Lb} \\ i_{Lc} \end{bmatrix} - \frac{1}{L_f}\begin{bmatrix} u_{ga} \\ u_{gb} \\ u_{gc} \end{bmatrix} + \frac{U_{dc}}{3L_f}\begin{bmatrix} 2 & -1 & -1 \\ -1 & 2 & -1 \\ -1 & -1 & 2 \end{bmatrix}\begin{bmatrix} s_a \\ s_b \\ s_c \end{bmatrix}. \tag{5}$$

After converting to *dq*-frame and ignoring the *o*-axis component, (5) can be written as

$$\dot{\boldsymbol{x}} = \boldsymbol{A}\boldsymbol{x} + \sqrt{\frac{2}{3}}\frac{U_{dc}}{3L_f}\boldsymbol{B}_k(t) + \boldsymbol{U}_{gdq} \tag{6}$$

where

$$\boldsymbol{x} = \begin{bmatrix} i_{Ld} \\ i_{Lq} \end{bmatrix}, \boldsymbol{A} = \begin{bmatrix} -\frac{R_f}{L_f} & \omega_o \\ -\omega_o & -\frac{R_f}{L_f} \end{bmatrix}, \boldsymbol{U}_{gdq} = -\frac{1}{L_f}\begin{bmatrix} u_{gd} \\ u_{gq} \end{bmatrix},$$

$$\boldsymbol{B}_k(t) = \begin{bmatrix} \cos(\omega_o t) & \cos(\omega_o t - \frac{2\pi}{3}) & \cos(\omega_o t + \frac{2\pi}{3}) \\ -\sin(\omega_o t) & -\sin(\omega_o t - \frac{2\pi}{3}) & -\sin(\omega_o t + \frac{2\pi}{3}) \end{bmatrix} \cdot \begin{bmatrix} 2S_a - S_b - S_c \\ 2S_b - S_a - S_c \\ 2S_c - S_a - S_b \end{bmatrix}$$

$\omega_{\rm o} = 100\pi$ is the grid voltage angular frequency.

B. Stroboscopic Mapping Modeling of Power Stage

Equation (6) is a linear time-varying state equation under each switching state, so the analytical expression of the state variable $\boldsymbol{x}$ can be derived as

$$\boldsymbol{x}(t) = e^{\boldsymbol{A}\cdot(t-t_0)}\boldsymbol{x}(t_0) + \int_{t_0}^{t}\sqrt{\frac{2}{3}}\frac{U_{dc}}{3L_f}e^{\boldsymbol{A}\cdot(t-\tau)}\boldsymbol{B}_k(\omega_o\tau)d\tau + [e^{\boldsymbol{A}\cdot(t-t_0)} - \boldsymbol{I}]\boldsymbol{A}^{-1}\boldsymbol{U}_{gdq}. \tag{7}$$

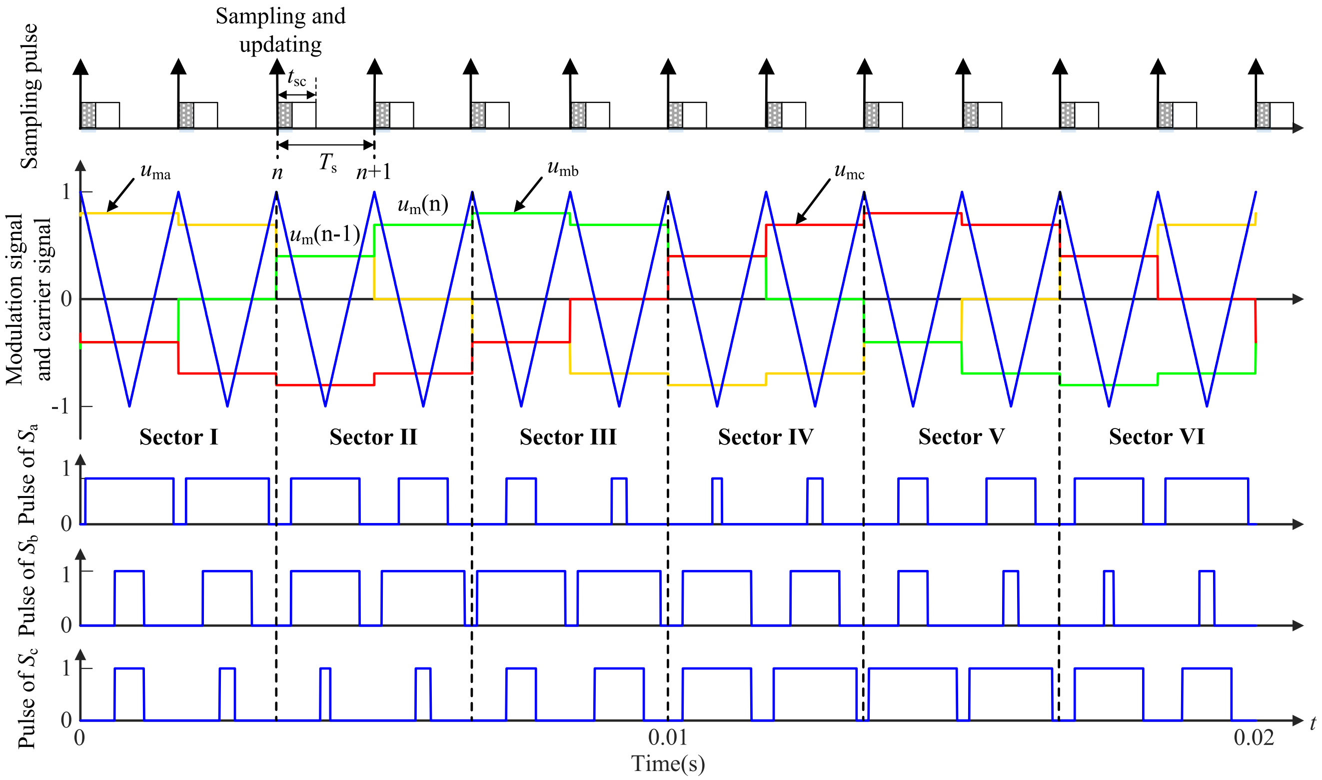

Fig. 6. Modulation schematic diagram of symmetric regular sampling.

TABLE II
*B*K(T) VALUE UNDER DIFFERENT SWITCHING STATES

The switching states($S_aS_bS_c$)	$\boldsymbol{B}_k(t)$
000/111	$\boldsymbol{B}_{0/7}(t)=\begin{bmatrix}0 & 0\end{bmatrix}^T$
100	$\boldsymbol{B}_1(t)=\begin{bmatrix}3\cos(\omega_o t) & -3\sin(\omega_o t)\end{bmatrix}^T$
110	$\boldsymbol{B}_2(t)=\begin{bmatrix}3\cos(\omega_o t-\frac{\pi}{3}) & -3\sin(\omega_o t-\frac{\pi}{3})\end{bmatrix}^T$
010	$\boldsymbol{B}_3(t)=\begin{bmatrix}-3\cos(\omega_o t+\frac{\pi}{3}) & 3\sin(\omega_o t+\frac{\pi}{3})\end{bmatrix}^T$
011	$\boldsymbol{B}_4(t)=\begin{bmatrix}-3\cos(\omega_o t) & 3\sin(\omega_o t)\end{bmatrix}^T$
001	$\boldsymbol{B}_5(t)=\begin{bmatrix}-3\cos(\omega_o t-\frac{\pi}{3}) & 3\sin(\omega_o t-\frac{\pi}{3})\end{bmatrix}^T$
101	$\boldsymbol{B}_6(t)=\begin{bmatrix}3\cos(\omega_o t+\frac{\pi}{3}) & -3\sin(\omega_o t+\frac{\pi}{3})\end{bmatrix}^T$

Since the three-phase two-level inverter has eight switching states, the values of B_k(t) in (7) under different switching states are shown in Table II.

The digital PWM adopts symmetrical regular sampling and sampling at the peak of triangular carrier wave, so the sampling period T_{sa} is consistent with the switching period T_s, and the modulation schematic diagram is shown in Fig. 6. Because the sampling and calculation time is t_{sc}, it is necessary to delay the calculated modulation signal by one beat and load it again [28], so the value of three-phase modulation signal in the nth switching period are u_{ma}(n-1), u_{mb}(n-1), and u_{mc}(n-1). It can be seen in Fig. 6 that the fundamental period can be divided into six different working areas according to the magnitude of the values between the three-phase modulated signals. In fact, this feature is similar to the six sectors when SVPWM is adopted [29]. Therefore, for convenience, we will just call the six work areas the six sectors. It can be found that the switching state type, sequence, and working time of the inverter are inconsistent in different sectors.

Let us take sector I as an example to calculate the stroboscopic mapping model of the power stage. The switching state type, sequence, and working time during any switching period in sector I are shown in Fig. 7. The solution of the state equation corresponding to the seven time periods in the *n*th switching period can be solved according to (7)

1) $t_n \to t_{n1}, \boldsymbol{B}_0(\omega_o t) = [0 \quad 0]^T$.

$$\boldsymbol{x}_{n1} = e^{\boldsymbol{A}\cdot t_1}\boldsymbol{x}_n + [e^{\boldsymbol{A}\cdot t_1} - \boldsymbol{I}]\boldsymbol{A}^{-1}\boldsymbol{U}_{gdq}. \tag{8}$$

2) $t_{n1} \to t_{n2}, \boldsymbol{B}_1(\omega_o t) = [3\cos(\omega_o t) \quad -3\sin(\omega_o t)]^T$.

$$\begin{aligned}\boldsymbol{x}_{n2} = e^{\boldsymbol{A}\cdot t_2}\boldsymbol{x}_{n1} &+ 3\boldsymbol{\alpha}[\beta\boldsymbol{G}_{\mathrm{I}1}(t_{n2}) + \boldsymbol{\gamma}\boldsymbol{G}_{\mathrm{I}2}(t_{n2}) \\ &- \beta e^{\boldsymbol{A}t_2}\boldsymbol{G}_{\mathrm{I}1}(t_{n1}) - \gamma e^{\boldsymbol{A}t_2}\boldsymbol{G}_{\mathrm{I}2}(t_{n1})] \\ &+ [e^{\boldsymbol{A}\cdot t_2} - \boldsymbol{I}]\boldsymbol{A}^{-1}\boldsymbol{U}_{gdq}\end{aligned} \tag{9}$$

where

$$\boldsymbol{\alpha} = \sqrt{\frac{2}{3}}\frac{U_{dc}}{3L_f}\cdot\left(\boldsymbol{I} + \frac{\boldsymbol{A}^2}{{\omega_o}^2}\right)^{-1}, \beta = \frac{1}{\omega_o}, \boldsymbol{\gamma} = \frac{\boldsymbol{A}}{{\omega_o}^2},$$

$$\boldsymbol{G}_{I1}(t) = \begin{bmatrix}\sin(\omega_o t)\\ \cos(\omega_o t)\end{bmatrix}, \boldsymbol{G}_{I2}(t) = \begin{bmatrix}-\cos(\omega_o t)\\ \sin(\omega_o t)\end{bmatrix}.$$

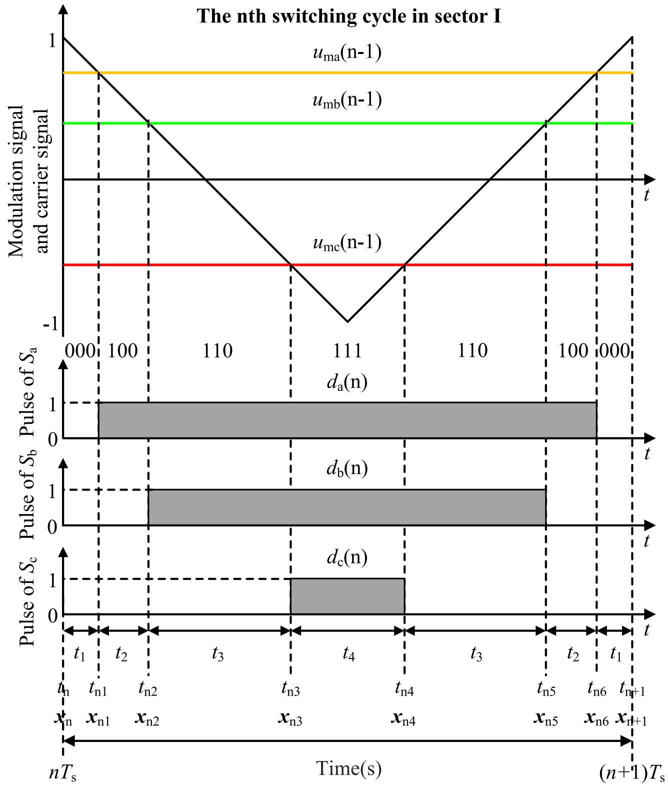

Fig. 7. Switching state of working in Sector I.

3) $t_{n2} \to t_{n3}, \boldsymbol{B}_2(\omega_o t) = [3\cos(\omega_o t - \frac{\pi}{3}) \; -3\sin(\omega_o t - \frac{\pi}{3})]^T$

$$\begin{aligned}\boldsymbol{x}_{n3} = e^{\boldsymbol{A}\cdot t_3}\boldsymbol{x}_{n2} &+ 3\boldsymbol{\alpha}[\beta\boldsymbol{G}_{I3}(t_{n3}) + \boldsymbol{\gamma}\boldsymbol{G}_{I4}(t_{n3})\\ &- \beta e^{\boldsymbol{A}t_3}\boldsymbol{G}_{I3}(t_{n2}) - \gamma e^{\boldsymbol{A}t_3}\boldsymbol{G}_{I4}(t_{n2})]\\ &+ [e^{\boldsymbol{A}\cdot t_3} - \boldsymbol{I}]\boldsymbol{A}^{-1}\boldsymbol{U}_{gdq} \end{aligned} \tag{10}$$

where $\boldsymbol{G}_{I3}(t) = \begin{bmatrix}\sin(\omega_o t - \frac{\pi}{3})\\ \cos(\omega_o t - \frac{\pi}{3})\end{bmatrix}$, $\boldsymbol{G}_{I4}(t) = \begin{bmatrix}-\cos(\omega_o t - \frac{\pi}{3})\\ \sin(\omega_o t - \frac{\pi}{3})\end{bmatrix}$.

4) $t_{n3} \to t_{n4}, \boldsymbol{B}_7(\omega_o t) = [0 \quad 0]^T$.

$$\boldsymbol{x}_{n4} = e^{\boldsymbol{A}\cdot t_4}\boldsymbol{x}_{n3} + [e^{\boldsymbol{A}\cdot t_4} - \boldsymbol{I}]\boldsymbol{A}^{-1}\boldsymbol{U}_{gdq}. \tag{11}$$

5) $t_{n4} \to t_{n5}, \boldsymbol{B}_2(\omega_o t) = [3\cos(\omega_o t - \frac{\pi}{3}) \; -3\sin(\omega_o t - \frac{\pi}{3})]^T$

$$\begin{aligned}\boldsymbol{x}_{n5} = e^{\boldsymbol{A}\cdot t_3}\boldsymbol{x}_{n4} &+ 3\boldsymbol{\alpha}[\beta\boldsymbol{G}_{I3}(t_{n5}) + \boldsymbol{\gamma}\boldsymbol{G}_{I4}(t_{n5})\\ &- \beta e^{\boldsymbol{A}t_3}\boldsymbol{G}_{I3}(t_{n4}) - \gamma e^{\boldsymbol{A}t_3}\boldsymbol{G}_{I4}(t_{n4})]\\ &+ [e^{\boldsymbol{A}\cdot t_3} - \boldsymbol{I}]\boldsymbol{A}^{-1}\boldsymbol{U}_{gdq}. \end{aligned} \tag{12}$$

6) $t_{n5} \to t_{n6}, \boldsymbol{B}_1(\omega_o t) = [3\cos(\omega_o t) \quad -3\sin(\omega_o t)]^T$

$$\begin{aligned}\boldsymbol{x}_{n6} = e^{\boldsymbol{A}\cdot t_2}\boldsymbol{x}_{n5} &+ 3\boldsymbol{\alpha}[\beta\boldsymbol{G}_{I1}(t_{n6}) + \boldsymbol{\gamma}\boldsymbol{G}_{I2}(t_{n6})\\ &- \beta e^{\boldsymbol{A}t_2}\boldsymbol{G}_{I1}(t_{n5}) - \gamma e^{\boldsymbol{A}t_2}\boldsymbol{G}_{I2}(t_{n5})]\\ &+ [e^{\boldsymbol{A}\cdot t_2} - \boldsymbol{I}]\boldsymbol{A}^{-1}\boldsymbol{U}_{gdq}. \end{aligned} \tag{13}$$

7) $t_{n6} \to t_{n+1}, \boldsymbol{B}_0(\omega_o t) = [0 \quad 0]^T$

$$\boldsymbol{x}_{n+1} = e^{\boldsymbol{A}\cdot t_1}\boldsymbol{x}_{n6} + [e^{\boldsymbol{A}\cdot t_1} - \boldsymbol{I}]\boldsymbol{A}^{-1}\boldsymbol{U}_{gdq}. \tag{14}$$

Equations (8)–(14) are the solutions of the state equations corresponding to seven time periods within any switching period in Sector I. Then, by iterating the solutions with each other, the expression of the stroboscopic mapping model for state variable $\boldsymbol{x}$ can be obtained as

$$\begin{aligned}\boldsymbol{x}_{n+1} = e^{\boldsymbol{A}\cdot T_s}\boldsymbol{x}_n &+ 3\boldsymbol{\alpha}(\boldsymbol{PT}_1 + \boldsymbol{PT}_2 + \boldsymbol{PT}_3 + \boldsymbol{PT}_4)\\ &+ [e^{\boldsymbol{A}\cdot T_s} - \boldsymbol{I}]\boldsymbol{A}^{-1}\boldsymbol{U}_{gdq}. \end{aligned} \tag{15}$$

Equation (15) is the stroboscopic mapping model established by taking Sector I as an example. It can follow the modeling principle and calculation method above to establish stroboscopic mapping models corresponding to the remaining five sectors. After calculation, the form of the expression obtained is the same as (15), which has three terms $\mathrm{e}^{\boldsymbol{A}T_\mathrm{s}}\boldsymbol{x}_\mathrm{n}$, $3\boldsymbol{\alpha}(\boldsymbol{PT}_1+\boldsymbol{PT}_2+\boldsymbol{PT}_3+\boldsymbol{PT}_4)$, and $[\mathrm{e}^{\boldsymbol{A}T_\mathrm{s}}\text{-}\boldsymbol{I}]\boldsymbol{A}^{-1}\boldsymbol{U}_\mathrm{gdq}$ (the calculation process will not be repeated here). Among them, the expressions $\mathrm{e}^{\boldsymbol{A}T_\mathrm{s}}$ and $[\mathrm{e}^{\boldsymbol{A}T_\mathrm{s}}\text{-}\boldsymbol{I}]\boldsymbol{A}^{-1}\boldsymbol{U}_\mathrm{gdq}$ are constant matrices, so in the expression of the stroboscopic mapping model under different sectors, these two terms are the same and can be expressed as

$$\begin{aligned} e^{\boldsymbol{A}\cdot T_s} &= e^{-\frac{R_f}{L_f}\cdot T_s}\begin{bmatrix}\cos(\omega_o T_s) & \sin(\omega_o T_s)\\ -\sin(\omega_o T_s) & \cos(\omega_o T_s)\end{bmatrix}\\ &= \begin{bmatrix}\sigma(1,1) & \sigma(1,2)\\ \sigma(2,1) & \sigma(2,2)\end{bmatrix} \end{aligned} \tag{16}$$

$$\boldsymbol{P} = [e^{\boldsymbol{A}\cdot T_s} - \boldsymbol{I}]\boldsymbol{A}^{-1}\boldsymbol{U}_{gdq} = \begin{bmatrix}\mathrm{P}(1,1)\\ \mathrm{P}(2,1)\end{bmatrix} \tag{17}$$

The expansion form of expression $3\boldsymbol{\alpha}(\boldsymbol{PT}_1 + \boldsymbol{PT}_2 + \boldsymbol{PT}_3 + \boldsymbol{PT}_4)$ is the same in the stroboscopic mapping models of different sectors, as shown in Appendix A. However, the expressions of $\boldsymbol{G}_1$(t), $\boldsymbol{G}_2$(t), $\boldsymbol{G}_3$(t), $\boldsymbol{G}_4$(t), t_1, t_2, t_3, t_4 and t_n, t_n1, …, t_n6, $t_\mathrm{n+1}$ are different in different sectors, see Appendix B for specific values. In fact, the expression $3\boldsymbol{\alpha}(\boldsymbol{PT}_1 + \boldsymbol{PT}_2 + \boldsymbol{PT}_3 + \boldsymbol{PT}_4)$ can be further simplified as shown in (18) shown at the bottom of the next page.

Then, by substituting (16), (17), and (18) into (15), the following expression can be obtained as

$$\begin{bmatrix}i_{Ld}(n+1)\\ i_{Lq}(n+1)\end{bmatrix} = \begin{bmatrix} \sigma(1,1)i_{Ld}(n)+\sigma(1,2)i_{Lq}(n)\\ +\left[sh\left(\frac{R_f T_s}{2L_f}d_a(n)\right)-sh\left(\frac{R_f T_s}{2L_f}d_b(n)\right)\right]\Lambda_1^n(1,1)\\ +\left[sh\left(\frac{R_f T_s}{2L_f}d_b(n)\right)-sh\left(\frac{R_f T_s}{2L_f}d_c(n)\right)\right]\Lambda_2^n(1,1)+\mathrm{P}(1,1)\\ \\ \sigma(2,1)i_{Ld}(n)+\sigma(2,2)i_{Lq}(n)\\ +\left[sh\left(\frac{R_f T_s}{2L_f}d_a(n)\right)-sh\left(\frac{R_f T_s}{2L_f}d_b(n)\right)\right]\Lambda_1^n(2,1)\\ +\left[sh\left(\frac{R_f T_s}{2L_f}d_b(n)\right)-sh\left(\frac{R_f T_s}{2L_f}d_c(n)\right)\right]\Lambda_2^n(2,1)+\mathrm{P}(2,1) \end{bmatrix}. \tag{19}$$

Compared with (15), (19) gives the stroboscopic mapping model in the analytical form of matrix elements.

As mentioned earlier, when the system operates in different sectors, the switch state sequence, order, and working time are different, therefore, it remains to be proven whether the stroboscopic mapping model is the same and unique. Here, only the model in Sector II is calculated in detail, and other sectors can follow the same calculation method. The stroboscopic mapping model expression in Sector II is obtained as

$$\begin{aligned}\boldsymbol{x}_{n+1} &= e^{\boldsymbol{A}\cdot T_s}\boldsymbol{x}_n + 3\boldsymbol{\alpha}(\boldsymbol{PT}_1 + \boldsymbol{PT}_2 + \boldsymbol{PT}_3 + \boldsymbol{PT}_4)\\ &\quad + [e^{\boldsymbol{A}\cdot T_s} - \boldsymbol{I}]\boldsymbol{A}^{-1}\boldsymbol{U}_{gdq}\end{aligned} \tag{20}$$

where the expressions of $e^{\boldsymbol{A}T_s}$ and $[e^{\boldsymbol{A}T_s}\text{-}\boldsymbol{I}]\boldsymbol{A}^{-1}\boldsymbol{U}_{\mathrm{gdq}}$ are shown respectively in (16) and (17). Therefore, only the second term $3\boldsymbol{\alpha}(\boldsymbol{PT}_1 + \boldsymbol{PT}_2 + \boldsymbol{PT}_3 + \boldsymbol{PT}_4)$ is simplified here. When the system operates in Sector II, the switching state type, sequence, and working time within any switching period are shown in Fig. 8. See Appendix B for the values of $\boldsymbol{G}_{\mathrm{II1}}(\mathrm{t})$, $\boldsymbol{G}_{\mathrm{II2}}(\mathrm{t})$, $\boldsymbol{G}_{\mathrm{II3}}(\mathrm{t})$, $\boldsymbol{G}_{\mathrm{II4}}(\mathrm{t})$ and t_1, t_2, t_3, t_4, and the values of $t_{\mathrm{n}}, t_{\mathrm{n1}}, \ldots, t_{\mathrm{n6}}, t_{\mathrm{n}+1}$ can be calculated as

$$\begin{cases} t_n = nT_s\\ t_{n1} = nT_s + t_1 = \frac{1}{2}[1 - d_b(n)]\cdot T_s + nT_s\\ t_{n2} = nT_s + t_1 + t_2 = \frac{1}{2}[1 - d_a(n)]\cdot T_s + nT_s\\ t_{n3} = nT_s + t_1 + t_2 + t_3 = \frac{1}{2}[1 - d_c(n)]\cdot T_s + nT_s\\ t_{n4} = nT_s + t_1 + t_2 + t_3 + t_4 = \frac{1}{2}[1 + d_c(n)]\cdot T_s + nT_s\\ t_{n5} = nT_s + t_1 + t_2 + t_3 + t_4 + t_3 = \frac{1}{2}[1 + d_a(n)]\cdot T_s + nT_s\\ t_{n6} = nT_s + t_1 + t_2 + t_3 + t_4 + t_3 + t_2\\ \qquad = \frac{1}{2}[1 + d_b(n)]\cdot T_s + nT_s\\ t_{n+1} = (T_s + nT_s) \end{cases} \tag{21}$$

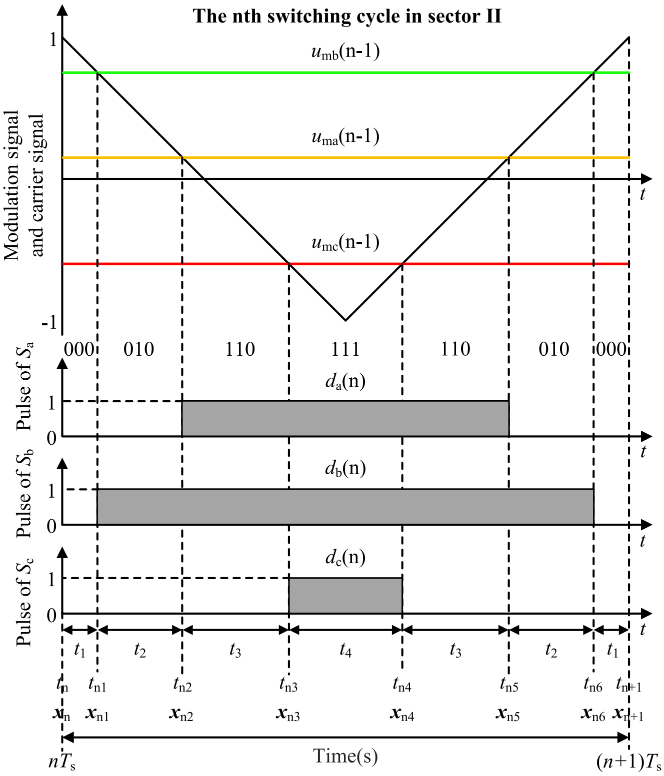

Fig. 8. Switching state of working in Sector II.

In Sector II, $3\boldsymbol{\alpha}(\boldsymbol{PT}_1 + \boldsymbol{PT}_2 + \boldsymbol{PT}_3 + \boldsymbol{PT}_4)$ can be simplified as shown in (22) shown at the bottom of the next page. It can be found that the final calculation result of (22) is equal to (18). Then, by substituting (16), (17), and (22) into (20), the expression of the stroboscopic mapping model working in Sector II in the analytical form of matrix elements is

---

$$\begin{aligned} &3\boldsymbol{\alpha}(PT_1 + PT_2 + PT_3 + PT_4)\\ &= 3\boldsymbol{\alpha}\{e^{-\frac{R_fT_s}{2L_f}}\left(e^{-\frac{R_fT_s}{2L_f}d_b} - e^{-\frac{R_fT_s}{2L_f}d_a} + e^{\frac{R_fT_s}{2L_f}d_a} - e^{\frac{R_fT_s}{2L_f}d_b}\right)[\beta\boldsymbol{G}_{I1}((n+1)T_s) + \boldsymbol{\gamma}\boldsymbol{G}_{I2}((n+1)T_s)]\\ &\quad + e^{-\frac{R_fT_s}{2L_f}}\left(e^{-\frac{R_fT_s}{2L_f}d_c} - e^{-\frac{R_fT_s}{2L_f}d_b} + e^{\frac{R_fT_s}{2L_f}d_b} - e^{\frac{R_fT_s}{2L_f}d_c}\right)[\beta\boldsymbol{G}_{I3}((n+1)T_s) + \boldsymbol{\gamma}\boldsymbol{G}_{I4}((n+1)T_s)]\\ &= \left[sh\left(\frac{R_fT_s}{2L_f}d_a\right) - sh\left(\frac{R_fT_s}{2L_f}d_b\right)\right]\cdot 6e^{-\frac{R_fT_s}{2L_f}}\cdot\boldsymbol{\alpha}\cdot[\beta\boldsymbol{G}_{I1}((n+1)T_s) + \boldsymbol{\gamma}\boldsymbol{G}_{I2}((n+1)T_s)]\\ &\quad + \left[sh\left(\frac{R_fT_s}{2L_f}d_b\right) - sh\left(\frac{R_fT_s}{2L_f}d_c\right)\right]\cdot 6e^{-\frac{R_fT_s}{2L_f}}\cdot\boldsymbol{\alpha}\cdot[\beta\boldsymbol{G}_{I3}((n+1)T_s) + \boldsymbol{\gamma}\boldsymbol{G}_{I4}((n+1)T_s)]\\ &= \left[sh\left(\frac{R_fT_s}{2L_f}d_a\right) - sh\left(\frac{R_fT_s}{2L_f}d_b\right)\right]\cdot\begin{bmatrix}\Lambda_1^n(1,1)\\ \Lambda_1^n(2,1)\end{bmatrix}\\ &\quad + \left[sh\left(\frac{R_fT_s}{2L_f}d_b\right) - sh\left(\frac{R_fT_s}{2L_f}d_c\right)\right]\cdot\begin{bmatrix}\Lambda_2^n(1,1)\\ \Lambda_2^n(2,1)\end{bmatrix} \end{aligned} \tag{18}$$

where $sh(x) = \frac{e^x - e^{-x}}{2}$ is hyperbolic sine function, and

$$\begin{bmatrix}\Lambda_1^n(1,1)\\ \Lambda_1^n(2,1)\end{bmatrix} = 6e^{-\frac{R_fT_s}{2L_f}}\cdot\boldsymbol{\alpha}\cdot[\beta\boldsymbol{G}_{\mathrm{I1}}((n+1)T_s) + \boldsymbol{\gamma}\boldsymbol{G}_{\mathrm{I2}}((n+1)T_s)]$$

$$\begin{bmatrix}\Lambda_2^n(1,1)\\ \Lambda_2^n(2,1)\end{bmatrix} = 6e^{-\frac{R_fT_s}{2L_f}}\cdot\boldsymbol{\alpha}\cdot[\beta\boldsymbol{G}_{\mathrm{I3}}((n+1)T_s) + \boldsymbol{\gamma}\boldsymbol{G}_{\mathrm{I4}}((n+1)T_s)]$$

obtained as

$$\begin{bmatrix} i_{Ld}(n+1) \\ i_{Lq}(n+1) \end{bmatrix} =$$

$$\begin{bmatrix} \sigma(1,1)i_{Ld}(n)+\sigma(1,2)i_{Lq}(n) \\ +\left[sh\left(\frac{R_fT_s}{2L_f}d_a(n)\right)-sh\left(\frac{R_fT_s}{2L_f}d_b(n)\right)\right]\Lambda_1^n(1,1) \\ +\left[sh\left(\frac{R_fT_s}{2L_f}d_b(n)\right)-sh\left(\frac{R_fT_s}{2L_f}d_c(n)\right)\right]\Lambda_2^n(1,1)+\mathrm{P}(1,1) \\ \\ \sigma(2,1)i_{Ld}(n)+\sigma(2,2)i_{Lq}(n) \\ +\left[sh\left(\frac{R_fT_s}{2L_f}d_a(n)\right)-sh\left(\frac{R_fT_s}{2L_f}d_b(n)\right)\right]\Lambda_1^n(2,1) \\ +\left[sh\left(\frac{R_fT_s}{2L_f}d_b(n)\right)-sh\left(\frac{R_fT_s}{2L_f}d_c(n)\right)\right]\Lambda_2^n(2,1)+\mathrm{P}(2,1) \end{bmatrix}. \tag{23}$$

Comparing (23) and (19), it can be seen that when the system operates in different sectors, although the switching state type, sequence, and working time are different, the expression of the stroboscopic mapping model is the same.

The previous text only compared Sector I and Sector II, for other sectors, the same result can still be obtained by following the modeling principle and computational simplification method introduced above, which will not be repeated here. It can be concluded that for three-phase inverters, in different sectors within one fundamental period, although the switching state type, sequence, and working time of the system are different, the expression of the stroboscopic mapping model is the same and unique.

C. Control Part Modeling

In Fig. 1, the control of grid-connected current is achieved using PI controller in the *dq*-frame. Here, the outputs u_{icond} and u_{iconq} of two integrators are selected as the state variables for the control part. The state equations for u_{icond} and u_{iconq} can be expressed as

$$\begin{cases} \frac{du_{\mathrm{icond}}}{dt} = k_i(i_{L d\mathrm{ref}} - i_{Ld}) \\ \frac{du_{\mathrm{iconq}}}{dt} = k_i(i_{L q\mathrm{ref}} - i_{Lq}) \end{cases}. \tag{24}$$

By using the forward difference to discretize (24), it can be obtained as

$$\begin{cases} u_{\mathrm{icond}}(n+1) = -k_i \cdot T_s \cdot i_{Ld}(n) + u_{\mathrm{icond}}(n) + k_i \cdot T_s \cdot i_{L d\mathrm{ref}} \\ u_{\mathrm{iconq}}(n+1) = -k_i \cdot T_s \cdot i_{Lq}(n) + u_{\mathrm{iconq}}(n) + k_i \cdot T_s \cdot i_{L q\mathrm{ref}} \end{cases}. \tag{25}$$

Due to delaying the calculated modulation signal by one beat before updating the loading, the three-phase modulation signal values in the *n*th switching period are $u_{\mathrm{ma}}(n\text{-}1)$, $u_{\mathrm{mb}}(n\text{-}1)$, and $u_{\mathrm{mc}}(n\text{-}1)$, respectively. Therefore, the three-phase duty cycle signal d_{a}, d_{b}, d_{c} can be expressed as

$$\begin{cases} d_a(n+1) = \frac{1}{2}[u_{ma}(n)+1] \\ d_b(n+1) = \frac{1}{2}[u_{mb}(n)+1] \\ d_c(n+1) = \frac{1}{2}[u_{mc}(n)+1] \end{cases} \tag{26}$$

In (26), the three-phase modulation signal u_{ma}, u_{mb}, and u_{mc} can be calculated according to Fig. 1, as shown in (27) shown at the bottom of the next page.

In Fig. 5, where the one-beat delay and nonlinear switching are reflected in (26) and (8)–(14), respectively. Here, the PWM saturation nonlinearity is accurately modeled. As shown in Fig. 5, u_{ma}(n), u_{mb}(n), and u_{mc}(n) are limited to the range [−1,1]. Taking u_{ma}(n) as an example, it can be expressed as

$$u_{ma}(n) = \begin{cases} -1 & u_{ma}(n) < -1 \\ u_{ma}(n) & -1 \le u_{ma}(n) \le 1 \\ 1 & u_{ma}(n) > 1 \end{cases}. \tag{28}$$

The relationship diagram between the duty cycle and modulation signal is shown in Fig. 9. The modulation signal is limited to the range $[-1, 1]$, which is equivalent to the duty cycle limited to the range [0, 1]. Therefore, the duty cycle of *a*-phase can be expressed as

$$d_a(n+1) = \begin{cases} 0 & u_{ma}(n) < -1 \\ \frac{1}{2}[u_{ma}(n)+1] & -1 \le u_{ma}(n) \le 1 \\ 1 & u_{ma}(n) > 1 \end{cases}. \tag{29}$$

Equation (29) represents the saturation nonlinearity in the form of a piecewise function. In order to facilitate subsequent model verification and bifurcation characteristics analysis, this

$$\begin{aligned} &3\boldsymbol{\alpha}(PT_1+PT_2+PT_3+PT_4) \\ &\quad = 3\boldsymbol{\alpha}\{e^{-\frac{R_fT_s}{2L_f}}\left(e^{-\frac{R_fT_s}{2L_f}d_a} - e^{-\frac{R_fT_s}{2L_f}d_b} + e^{\frac{R_fT_s}{2L_f}d_b} - e^{\frac{R_fT_s}{2L_f}d_a}\right)[\beta\boldsymbol{G}_{I1}((n+1)T_s)+\boldsymbol{\gamma}\boldsymbol{G}_{I2}((n+1)T_s)] \\ &\qquad + e^{-\frac{R_fT_s}{2L_f}}\left(e^{-\frac{R_fT_s}{2L_f}d_c} - e^{-\frac{R_fT_s}{2L_f}d_a} + e^{\frac{R_fT_s}{2L_f}d_a} - e^{\frac{R_fT_s}{2L_f}d_c}\right)[\beta\boldsymbol{G}_{I3}((n+1)T_s)+\boldsymbol{\gamma}\boldsymbol{G}_{I4}((n+1)T_s)]\} \\ &\quad = \left[sh\left(\frac{R_fT_s}{2L_f}d_a\right) - sh\left(\frac{R_fT_s}{2L_f}d_b\right)\right]\cdot 6e^{-\frac{R_fT_s}{2L_f}}\cdot\boldsymbol{\alpha}\cdot[\beta\boldsymbol{G}_{I1}((n+1)T_s)+\boldsymbol{\gamma}\boldsymbol{G}_{I2}((n+1)T_s)] \\ &\qquad + \left[sh\left(\frac{R_fT_s}{2L_f}d_b\right) - sh\left(\frac{R_fT_s}{2L_f}d_c\right)\right]\cdot 6e^{-\frac{R_fT_s}{2L_f}}\cdot\boldsymbol{\alpha}\cdot[\beta\boldsymbol{G}_{I3}((n+1)T_s)+\boldsymbol{\gamma}\boldsymbol{G}_{I4}((n+1)T_s)] \\ &\quad = \left[sh\left(\frac{R_fT_s}{2L_f}d_a\right) - sh\left(\frac{R_fT_s}{2L_f}d_b\right)\right]\cdot\begin{bmatrix}\Lambda_1^n(1,1)\\ \Lambda_1^n(2,1)\end{bmatrix} + \left[sh\left(\frac{R_fT_s}{2L_f}d_b\right) - sh\left(\frac{R_fT_s}{2L_f}d_c\right)\right]\cdot\begin{bmatrix}\Lambda_2^n(1,1)\\ \Lambda_2^n(2,1)\end{bmatrix}. \end{aligned} \tag{22}$$

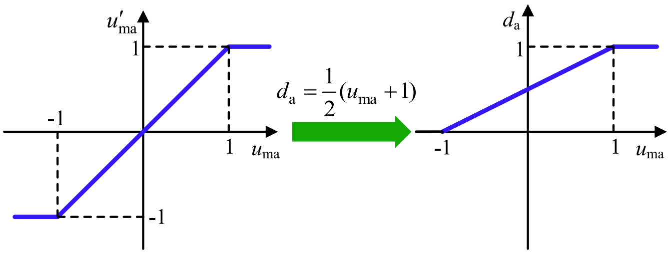

Fig. 9. Schematic diagram of duty cycle saturation.

article uses the step function $\varepsilon(x)$ to represent the saturation nonlinearity of PWM in analytical form, so (29) can be further rewritten as

$$\begin{aligned} d_a(n+1) &= \frac{1}{2}[u_{ma}(n)+1]\cdot[\varepsilon(u_{ma}(n)+1) \\ &\quad -\varepsilon(u_{ma}(n)-1)] + \varepsilon(u_{ma}(n)-1) \\ &= \frac{1}{2}[u_{ma}(n)+1]\cdot\varepsilon(u_{ma}(n)+1) \\ &\quad -\frac{1}{2}[u_{ma}(n)-1]\cdot\varepsilon(u_{ma}(n)-1). \end{aligned} \tag{30}$$

Therefore, the three-phase duty cycle signal can be expressed as shown in (31) shown at the bottom of the this page.

It can be seen that the use of step functions can accurately model the hard nonlinearity of PWM saturation limiting without any approximation. So far, (19), (25), (27), and (31). constitute the stroboscopic mapping model of the digitally controlled grid-connected inverter system shown in Fig. 1.

IV. MODEL VALIDATION AND BIFURCATION CHARACTERISTICS ANALYSIS

This section conducts numerical simulation on the stroboscopic mapping model established in Section III and compares it with the simulation model results in MATLAB/Simulink to verify the accuracy of the stroboscopic mapping model established in this article. Then, with the help of the bifurcation diagram and the root locus of Jacobian matrix, the bifurcation characteristics when PWM saturates under the condition of increasing controller proportional coefficient k_p and grid voltage swell are analyzed, revealing the essential reasons for grid-connected current oscillation and its relationship with PWM saturation, and the bifurcation boundary is accurately predicted.

A. *Numerical Simulation Verification*

Based on the system parameters in Table I, the simulation model shown in Fig. 1 is built on the MATLAB/Simulink platform. At the same time, the numerical simulation is conducted on the established stroboscopic mapping model, and the accuracy of the stroboscopic mapping model is verified in both the time and frequency domains. Fig. 10 takes the *d*/*q*-axis components of grid-connected current as an example to compare the time-domain waveform of the two models under the same working conditions as Figs. 2 and 3. It can be seen that both in the steady-state stage and the transient transition stage, the discrete sampling points of the stroboscopic mapping model completely coincide with the stepped waveform of the Simulink model.

Fig. 11 compares the spectrum of the output current of the two models under the working conditions of increasing k_p and grid voltage swell. In Fig. 11(a), it can be seen that the harmonic distribution of the stroboscopic mapping model is almost identical to that of the Simulink simulation model, with only 0.87% error in their THD values, which is caused by the FFT calculation error inside the MATLAB simulation software. Note: Due to the fact that the stroboscopic mapping model is based on the switching period as the sampling period, the switching frequency here is 10 kHz. According to the Shannon sampling theorem, the stroboscopic mapping model can perfectly reproduce the original signal within 5 kHz, so the spectrum here only displays harmonics within 5 kHz.

Fig. 11(b) compares the spectrums of the output current of the two models before and after grid voltage swell. It can be seen that the spectrum of the stroboscopic mapping model is almost identical to that of the Simulink simulation model. Comparing the spectra of grid-connected currents at $k_p = 40$ and $U_g = 1.2$ p.u. in Fig. 11, it can be seen that the frequency of oscillation harmonics in the grid-connected currents is different in these two cases, this also confirms the different oscillation frequencies of the *d*/*q*-axis current in Figs. 2 and 3.

To sum up, the stroboscopic mapping model has high model accuracy and can perfectly describe such a strong nonlinear system as grid-connected inverters whether the system is in normal operation or when PWM saturation occurs.

$$\begin{bmatrix} u_{ma}(n) \\ u_{mb}(n) \\ u_{mc}(n) \end{bmatrix} = \frac{2}{U_{dc}}\sqrt{\frac{2}{3}}\begin{bmatrix} \cos(\omega_o nT_s) & -\sin(\omega_o nT_s) \\ \cos(\omega_o nT_s - \frac{2\pi}{3}) & -\sin(\omega_o nT_s - \frac{2\pi}{3}) \\ \cos(\omega_o nT_s + \frac{2\pi}{3}) & -\sin(\omega_o nT_s + \frac{2\pi}{3}) \end{bmatrix} \cdot \left(\begin{bmatrix} -k_p & -\omega_o L_f \\ \omega_o L_f & -k_p \end{bmatrix} \boldsymbol{x}(n) + \begin{bmatrix} u_{icond}(n) \\ u_{iconq}(n) \end{bmatrix} + \begin{bmatrix} u_{gd} \\ u_{gq} \end{bmatrix} + k_p \begin{bmatrix} i_{Ldref} \\ i_{Lqref} \end{bmatrix} \right). \tag{27}$$

$$\begin{bmatrix} d_a(n+1) \\ d_b(n+1) \\ d_c(n+1) \end{bmatrix} = \begin{bmatrix} \frac{1}{2}[u_{ma}(n)+1]\cdot\varepsilon(u_{ma}(n)+1) - \frac{1}{2}[u_{ma}(n)-1]\cdot\varepsilon(u_{ma}(n)-1) \\ \frac{1}{2}[u_{mb}(n)+1]\cdot\varepsilon(u_{mb}(n)+1) - \frac{1}{2}[u_{mb}(n)-1]\cdot\varepsilon(u_{mb}(n)-1) \\ \frac{1}{2}[u_{mc}(n)+1]\cdot\varepsilon(u_{mc}(n)+1) - \frac{1}{2}[u_{mc}(n)-1]\cdot\varepsilon(u_{mc}(n)-1) \end{bmatrix}. \tag{31}$$

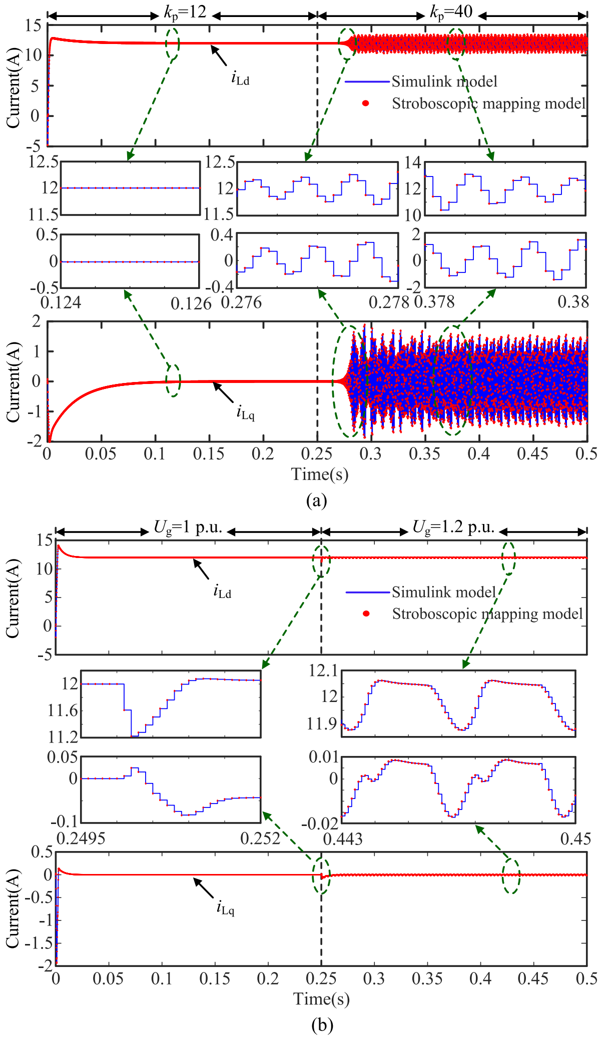

(a)

(b)

Fig. 10. Model comparison in the time domain. (a) Increase k_p. (b) Grid voltage swell.

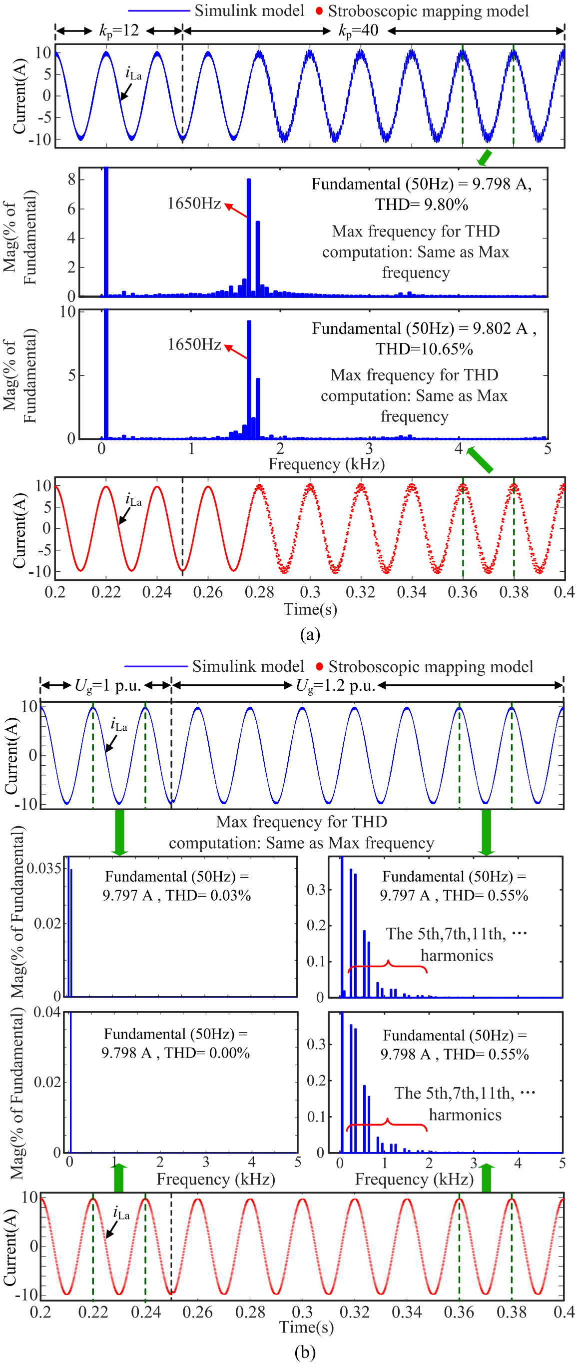

(a)

(b)

Fig. 11. Model comparison in the frequency domain. (a) Increase k_p. (b) Grid voltage swell.

B. Analysis of Bifurcation Characteristics

The following analyzes the bifurcation characteristics of the system under the two PWM saturation conditions described above, and explains the essential reasons for grid-connected current oscillation from the perspective of bifurcation.

Fig. 12 shows the bifurcation diagrams of k_p-i_{Ld} and k_p-i_{La}, with k_p as the bifurcation parameter. The bifurcation diagram of k_p-i_{La} is drawn by continuously sampling the values at the peak of i_{La}. The incremental step size of k_p is 0.1. It can be seen that the bifurcation point of k_p is 34.9, that is, when k_p is greater than this value, the system will experience the super-critical Hopf bifurcation, thus the grid-connected current will be distorted, showing sustained constant-amplitude oscillations, as shown in Fig. 2 above. In essence, this is a nonlinear system experiencing its unique self-excited oscillation, forming a stable limit cycle, as shown in Fig. 13.

In Fig. 13(a), the system operates stably, and the *d*/*q*-axis components of the grid-connected current operate at its reference value, so the phase trajectory is a point. In Fig. 13(b), the fixed point of the system becomes statically unstable, forming a stable limit cycle, so the grid-connected current exhibits a sustained constant-amplitude oscillation.

Fig. 14 shows the bifurcation diagrams of U_g-i_{Ld} and U_g-i_{La}, with the RMS value U_g of grid voltage as bifurcation parameter. Similarly, the bifurcation diagram of U_g-i_{La} is drawn by continuously sampling the values at the peak of i_{La}. The incremental step size of U_g is 0.1. it can be seen that when U_g is greater than 47, that is, the amplitude U_{gm} of grid voltage is greater than $47\sqrt{2}$, the bifurcation diagram of U_g-i_{Ld} is no longer a straight line, while the bifurcation diagram of U_g-i_{La} shows that the peak

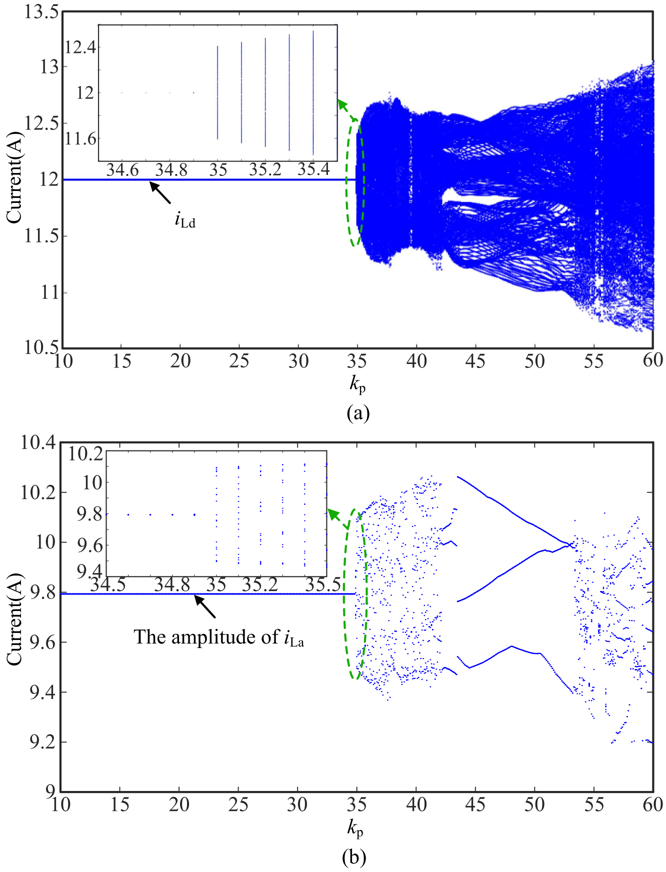

(a)

(b)

Fig. 12. Bifurcation diagram with changes in k_{p}. (a) Bifurcation diagram of k_{p}-i_{Ld}. (b) Bifurcation diagram of k_{p}-i_{La}.

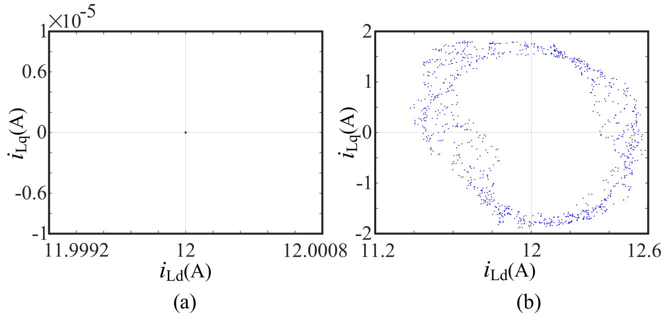

(a)

(b)

Fig. 13. Phase plane diagram of i_{Ld}-i_{Lq}. (a) $k_{\mathrm{p}} = 12$. (b) $k_{\mathrm{p}} = 40$.

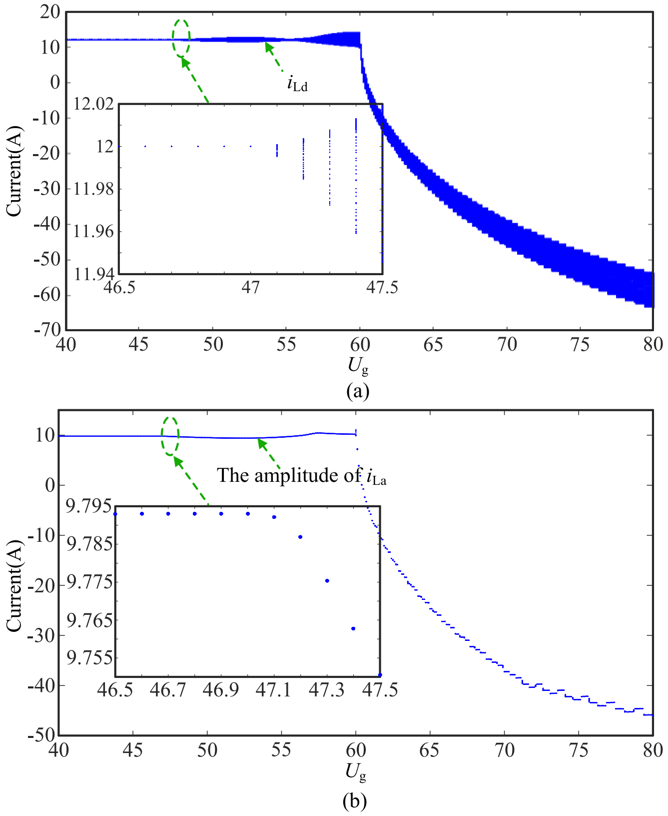

(a)

(b)

Fig. 14. Bifurcation diagram with changes in U_{g}. (a) Bifurcation diagram of U_g-i_{Ld}. (b) Bifurcation diagram of U_{g}-i_{La}.

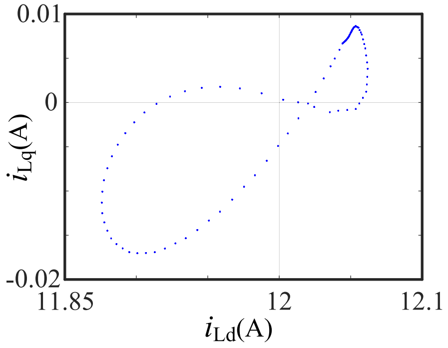

Fig. 15. Phase plane diagram of i_{Ld}-i_{Lq} at $U_{\mathrm{g}} = 1.2$ p.u.

value of i_{La} gradually decreases with the increase of U_{g}, but the bifurcation diagram of U_{g}-i_{La} is still a line.

The phase plane diagram of i_{Ld}-i_{Lq} at $U_{\mathrm{g}} = 1.2$ p.u. is shown in Fig. 15. It can be seen that the phase trajectory is an irregular closed curve, not a limit cycle, so the system does not have bifurcation. Since the bifurcation diagrams and phase plane diagram are drawn based on the numerical simulation results of the accurate stroboscopic mapping model, according to the characteristics of Figs. 14 and 15, it can be determined that when U_{gm} is greater than its critical value, although the grid-connected current is distorted, this is not caused by the bifurcation of the system, but the output voltage u_{ao} of grid-connected inverter increases with the increase of grid voltage, resulting in PWM over-modulation. This case is explained in detail later by the root locus of Jacobian matrix and phasor diagram.

The critical values of the bifurcation parameters k_{p} and U_{g} are obtained from the bifurcation diagram above. Fig. 16 shows the PWM saturation situation when the bifurcation parameters k_{p} and U_{g} are near their critical values. It can be seen that when k_{p} or U_{g} is less than its critical value, PWM is not saturated, that is, there is no case of overmodulation. When it exceeds its critical value, PWM will exhibit saturation characteristics. Therefore, by solving the root locus of Jacobian matrix, the critical values of k_{p} and U_{g} can also be obtained, and the bifurcation type can

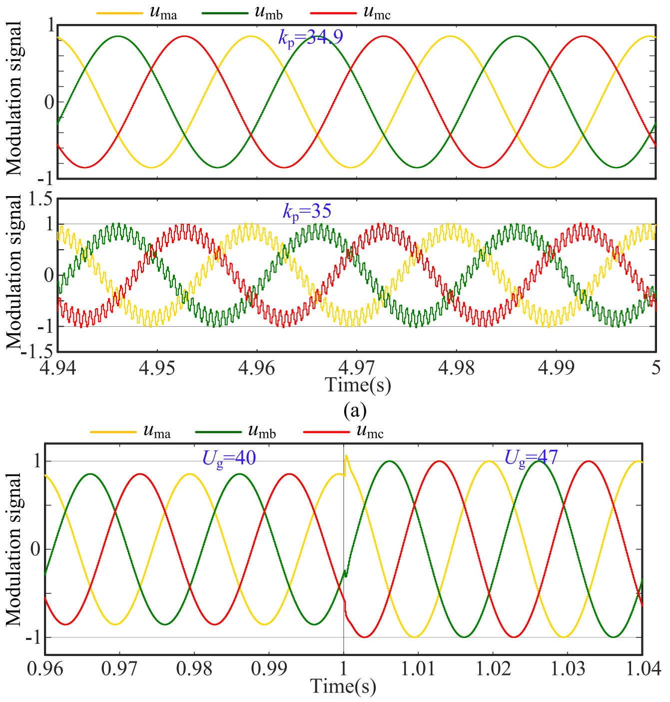

(a)

(b)

Fig. 16. PWM saturation situation near the critical value. (a) Near the critical value of $k_{\rm p}$. (b) Near the critical value of $U_{\rm g}$.

be determined by the position where the root locus crosses unit circle. Note: Since solving the Jacobi matrix requires solving the partial derivative of system's state equation, the saturation characteristics in PWM is not considered for the time being, that is, the step function in the stroboscopic mapping model is ignored.

The stroboscopic mapping model established in this article (ignoring the PWM saturation) is abbreviated as

$$\boldsymbol{x'}(n+1) = \boldsymbol{F}[\boldsymbol{x'}(n), \boldsymbol{P}, n] \tag{32}$$

where $\boldsymbol{x'}(n) = [i_{Ld}(n) \quad i_{Lq}(n) \quad u_{\rm icond}(n) \quad u_{\rm iconq}(n) \quad d_a(n) \quad d_b(n) \quad d_c(n)]^T$.

Calculating the Jacobian matrix of (32), and its specific expression is shown in Appendix C. Due to the fact that the established stroboscopic mapping model is a nonlinear and time-varying differential state equation, the Jacobian matrix is related to the state variables $d_{\rm a}$, $d_{\rm b}$, $d_{\rm c}$, and the sequence number n (i.e., sampling time) of the fixed point $\boldsymbol{x}_0{}'$.

It is known from the above-mentioned bifurcation diagram that the bifurcation type occurring in this system is Hopf bifurcation. Therefore, although there are $f_{\rm sw}/f_{\rm o}$ fixed points in a fundamental period, the stability types of these fixed points are consistent, so only the stability of any one of them needs to be analyzed here, and the sequence number n of the fixed point $\boldsymbol{x}_0{}'$ is taken as 50. Such that

$$\boldsymbol{x'}(n+1) = \boldsymbol{x'}(n). \tag{33}$$

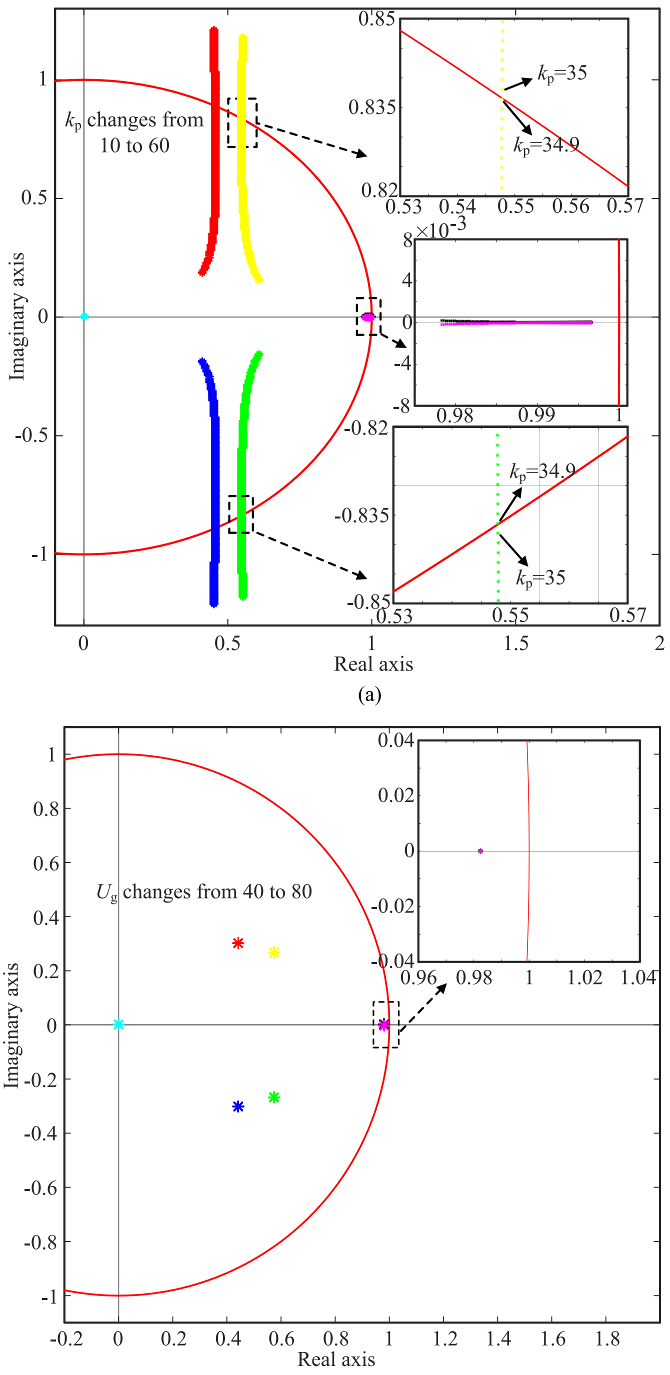

(a)

(b)

Fig. 17. Root locus of Jacobian matrix. (a) Root locus with $k_{\rm p}$ changes. (b) Root locus with $U_{\rm g}$ changes.

Using numerical algorithms to solve the nonlinear equation system (33), the fixed point $\boldsymbol{x}_0{}'$ of (32) is obtained. Then, substituting it into the Jacobian matrix. Finally, by solving the eigenvalues of Jacobian matrix and determining the relationship between the position of all eigenvalues and unit circle, the stable type of $\boldsymbol{x}_0{}'$ can be determined.

Fig. 17 shows the root locus of Jacobian matrix with changes in $k_{\rm p}$ and $U_{\rm g}$, the critical value of $k_{\rm p}$ and $U_{\rm g}$ can be obtained, and by observing the position where the root locus crosses the unit circle, the type of bifurcation in the system can be determined.

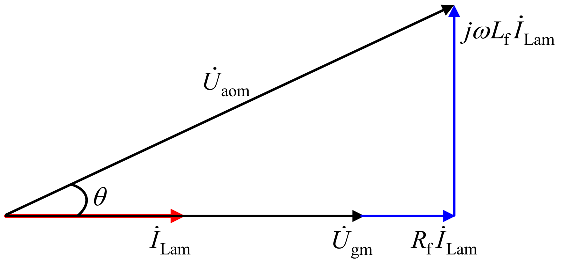

Fig. 18. AC side voltage phasor diagram in steady-state operation.

In Fig. 17(a), it can be seen that as k_{p} gradually increases, the root locus of Jacobian matrix passes through the right half of unit circle, causing the fixed point to become unstable and the system to exhibit Hopf bifurcation, resulting in the oscillation of the grid-connected current. It can also be seen that when k_{p} is greater than 34.9, the conjugate eigenvalues are located outside the unit circle, which is the critical value of k_{p}. These are consistent with the conclusions drawn from the bifurcation diagram above. In addition, it can be seen from Appendix C that the elements of Jacobian matrix are related to k_{p}, that is, k_{p} affects the stability of the fixed points of the system.

In Fig. 17(b), it can be seen that as U_{g} gradually increases, the position of eigenvalues remains unchanged and remains within the unit circle. Therefore, it can be concluded that when the grid voltage swell causes the PWM saturation and grid-connected current oscillations, as shown in Fig. 3, which is not caused by the static instability of the system's fixed point leading to bifurcation. This is consistent with the conclusion drawn from the bifurcation diagram above. In addition, it can be seen from Appendix C that the elements of the Jacobian matrix are independent of the grid voltage, meaning that the grid voltage does not affect the stability of the system's fixed points.

C. Relationship Between Sustained Constant-Amplitude Oscillation and PWM Saturation

At the ac side of the grid-connected inverter, the amplitude phasor of grid voltage is $\dot{U}_{gm}$, the amplitude phasor of filter voltage is $\dot{U}_{fm}$, the amplitude phasor of output voltage on the ac side is $\dot{U}_{aom}$, and the amplitude phasor of grid-connected current is $\dot{I}_{Lam}$, their expressions are shown in (34). When the system enters steady-state operation, according to the KVL law, the phasor diagram shown in Fig. 18 can be obtained. Since the voltage phasor diagram is a right triangle, the relationship expression between the modulus of ac side voltage phasor can be obtained, as shown in (35).

$$\begin{cases} \dot{U}_{gm} = \sqrt{2}U_g\angle 0^\circ \\ \dot{U}_{fm} = R_f\dot{I}_{Lam} + j\omega_o L_f\dot{I}_{Lam} \\ \dot{U}_{aom} = m_a\frac{U_{dc}}{2}\angle\theta \\ \dot{I}_{Lam} = \sqrt{\frac{2}{3}}i_{Ldref}\angle 0^\circ \end{cases} \tag{34}$$

$$\left|\dot{U}_{aom}\right|^2 = \left|\dot{U}_{gm} + R_f\dot{I}_{Lam}\right|^2 + \left|j\omega_o L_f\dot{I}_{Lam}\right|^2$$

$$\Rightarrow \left(m_a\frac{U_{dc}}{2}\right)^2 = \left(\sqrt{2}U_g + \sqrt{\frac{2}{3}}i_{Ldref}R_f\right)^2 + \left(\sqrt{\frac{2}{3}}i_{Ldref}\omega_o L_f\right)^2 \tag{35}$$

where m_{a} is the amplitude modulation index of a-phase.

Substituting the parameters in Table I into (35) and making m_{a} take the maximum value, that is, $m_{\mathrm{a}} = 1$. Then $U_{\mathrm{g}} = 47.03$ is obtained by solving (35), which is consistent with the critical value obtained from the bifurcation diagram above. Therefore, when U_{g} is greater than this value, PWM is saturated, that is $m_{\mathrm{a}} > 1$. As is well known, when PWM occurs overmodulation, the content of low order harmonics (5th, 7th, 11th …) in the output voltage u_{ao} of the inverter will increase, resulting in an increase in the content of low order harmonics in the grid-connected current. Due to the low-pass filtering characteristics of the entire control loop (sampling, PI controller, filter), the closed-loop control system has a bandwidth, so these low-order harmonics will not be attenuated and will always exist in the closed-loop system of the grid-connected inverter [as shown in Fig. 11(b)], causing the grid-connected current to exhibit sustained constant-amplitude oscillation. For the case shown in Fig. 3, this is the essential reason for grid-connected current oscillation or the relationship between grid-connected current oscillation and PMW saturation.

From the previous analysis, it has been found that the root cause for the grid-connected current oscillation shown in Fig. 2 is that when k_{p} exceeds its critical value of 34.9, the system's fixed point becomes statically unstable, and the system undergoes super-critical Hopf bifurcation. Meanwhile, PWM also experiences saturation. Let us explore the relationship between the sustained oscillation of grid-connected current and PWM saturation in this situation.

As can be seen from the PWM equivalent model shown in Fig. 5, the saturation limiting characteristic of PWM is its inherent property, so in Simulink simulation and experiments, it is impossible to separately remove the saturation limiting link in PWM to observe the dynamic behaviors of the system. However, in the stroboscopic mapping model, the saturation limiting characteristics of PWM can be ignored for now, the simulation waveform when k_{p} is greater than 34.9 can be observed by numerical simulation, and compared with the simulation waveform of the Simulink model under the same parameters.

Here are the Simulink simulation waveforms of the modulation signal and grid-connected current at $k_{\mathrm{p}} = 35$, as well as the numerical simulation waveforms of the stroboscopic mapping model without considering PWM saturation under the same parameters, as shown in Fig. 19. It can be seen that in Fig. 19(a), both the grid-connected current and modulation signal exhibit sustained constant-amplitude oscillation, whereas in Fig. 19(b), both the grid-connected current and modulation signal oscillate and diverge. Through comparison, it can be found that when the parameters of the grid-connected inverter system change, causing static instability of the system's fixed point, the grid-connected current and modulation signal will oscillate and

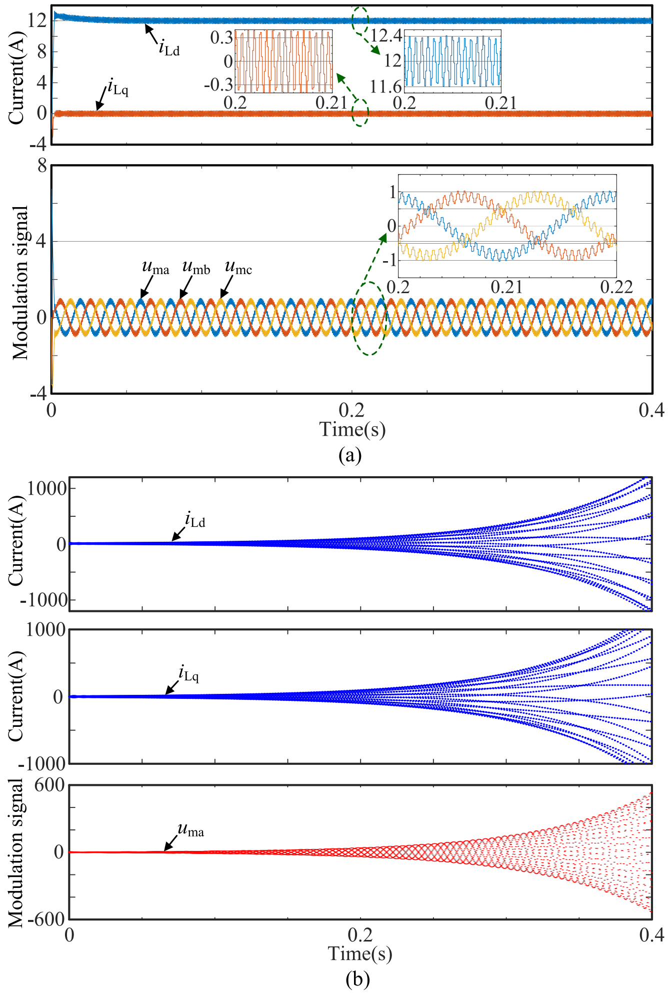

Fig. 19. Simulation waveforms of the two models when $k_p = 35$. (a) Simulink model. (b) Stroboscopic mapping model without considering PWM saturation.

diverge. However, due to the inherent saturation limiting nonlinearity of PWM, the system will undergo super-critical Hopf bifurcation, and the grid-connected current will exhibit sustained constant-amplitude oscillation. In fact, this is a nonlinear system that experiences its unique self-excited oscillation, forming a stable limit cycle.

In summary, taking the sustained constant-amplitude oscillation of grid-connected current caused by the increase of k_p or grid voltage swell as an example, based on the stroboscopic mapping model, the essential reasons for the oscillation of grid-connected current under these two working conditions were clarified using the analysis method of bifurcation diagram and the root locus of Jacobian matrix.

1) When k_p increases beyond the critical value, the fixed point of the system becomes unstable, the grid-connected current and modulation signal will oscillate and diverge. However, due to the inherent saturation limiting nonlinearity of PWM, the system undergoes super-critical Hopf bifurcation, forming a stable limit cycle, causing the grid-connected current to exhibit sustained constant-amplitude oscillation, and PWM becomes saturated.

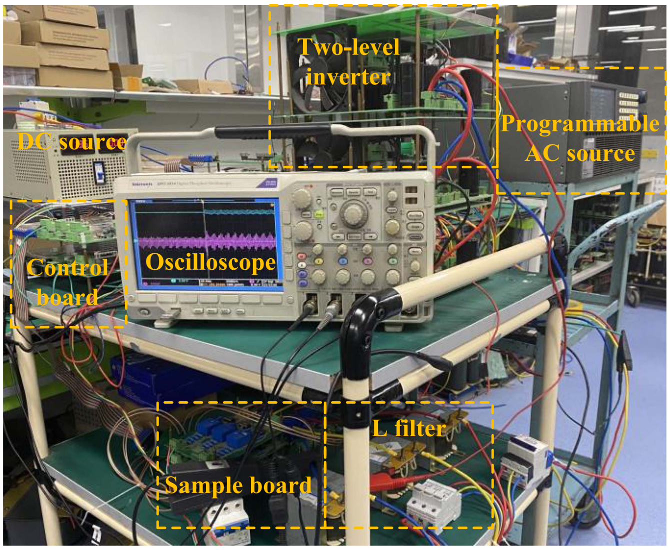

Fig. 20. Experimental platform.

2) When the grid voltage suddenly swells beyond the critical value, in order to ensure that each voltage phasors on the ac side still meets the phasor diagram shown in Fig. 16, due to the automatic adjustment of closed-loop control, the modulation signal will also increase, resulting in PWM overmodulation. At this time, the content of low-order harmonics (5th, 7th, 11th …) in the output voltage u_{ao} and grid-connected current will increase. Moreover, due to the low-pass filtering characteristics of the entire closed-loop control system, these low-order harmonics will not be attenuated and will always exist in the system, causing the grid-connected current to exhibit sustained constant-amplitude oscillation, but the fixed point of the system is still stable and does not undergo bifurcation.

V. EXPERIMENTAL VERIFICATION

The experimental platform shown in Fig. 20 of a three-phase grid-connected inverter is built, to further verify the correctness of the above theoretical analysis. Using PRE1510M programmable ac power supply to simulate the power grid. PWM signal generation, current, and voltage signal sampling are all realized by FPGA of XC6SLX25. Coordinate transformation, current closed-loop control, and other functions are completed by TMS320C25346 DSP. The experimental control strategy and PI controller discretization method are consistent with the theoretical part.

When $k_p = 40$, the grid-connected current and its spectrum, as well as the three-phase modulation signal, are shown in Fig. 21. In Fig. 21(a), it can be seen that the system undergoes the super-critical Hopf bifurcation, and the grid-connected current exhibits sustained constant-amplitude oscillation. Fig. 21(b) shows the spectrum of the grid-connected current, indicating that the fundamental amplitude of the grid-connected current is 10.02 A, and the oscillation frequency is 1550 Hz. In Fig. 21(c), the three-phase modulation signal undergoes sustained oscillation

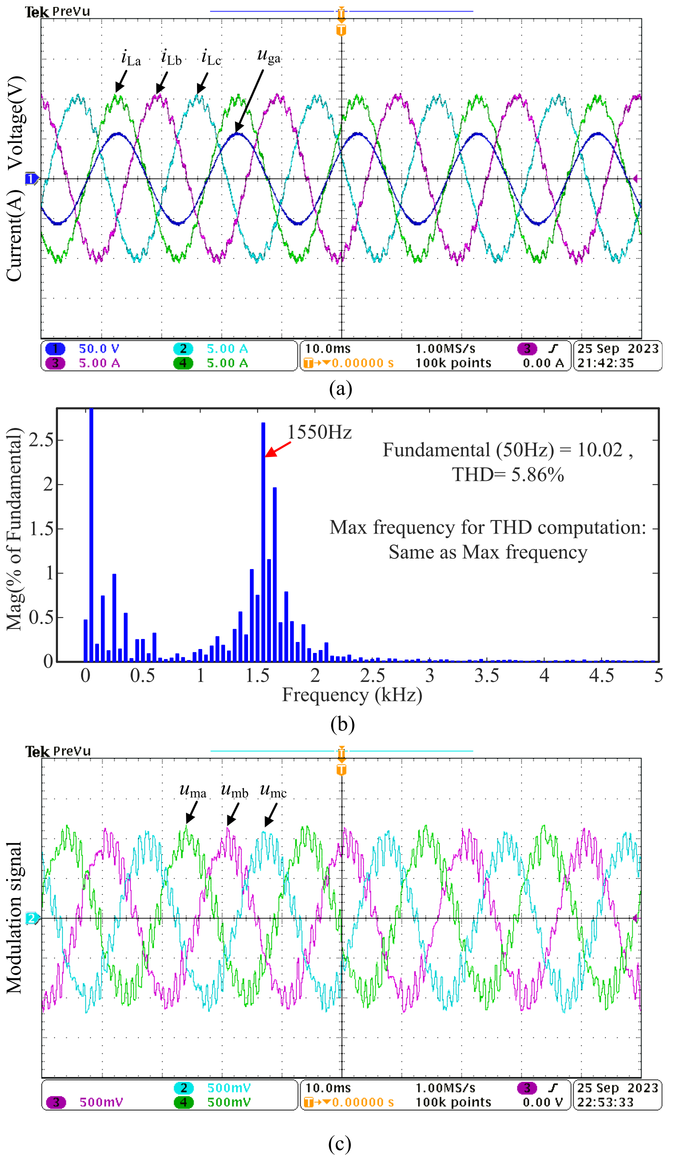

Fig. 21. Experimental waveform when $k_p = 40$. (a) Three-phase grid-connected current and grid voltage. (b) Grid-connected current spectrum. (c) Three-phase modulation signal.

and overmodulation. These experimental results are basically consistent with the above theoretical and simulation analysis results.

Fig. 22 shows the experimental waveform of the grid-connected current and its spectrum, as well as the three-phase modulation signal, when the grid voltage swells by 20%. It can be seen that when grid voltage swells, the grid-connected current undergoes oscillation, and the three-phase modulation signal is overmodulated. In Fig. 22(b), after the grid voltage swell, the 5th, 7th, and 11th harmonic content of grid-connected current increases, while before the grid voltage swell, the 5th, 7th, and 11th harmonics of grid-connected current are mainly caused by dead-time factors in PWM. After comprehensive consideration, it can be seen that the experimental results verify the correctness of the previous theoretical and simulation analysis. The

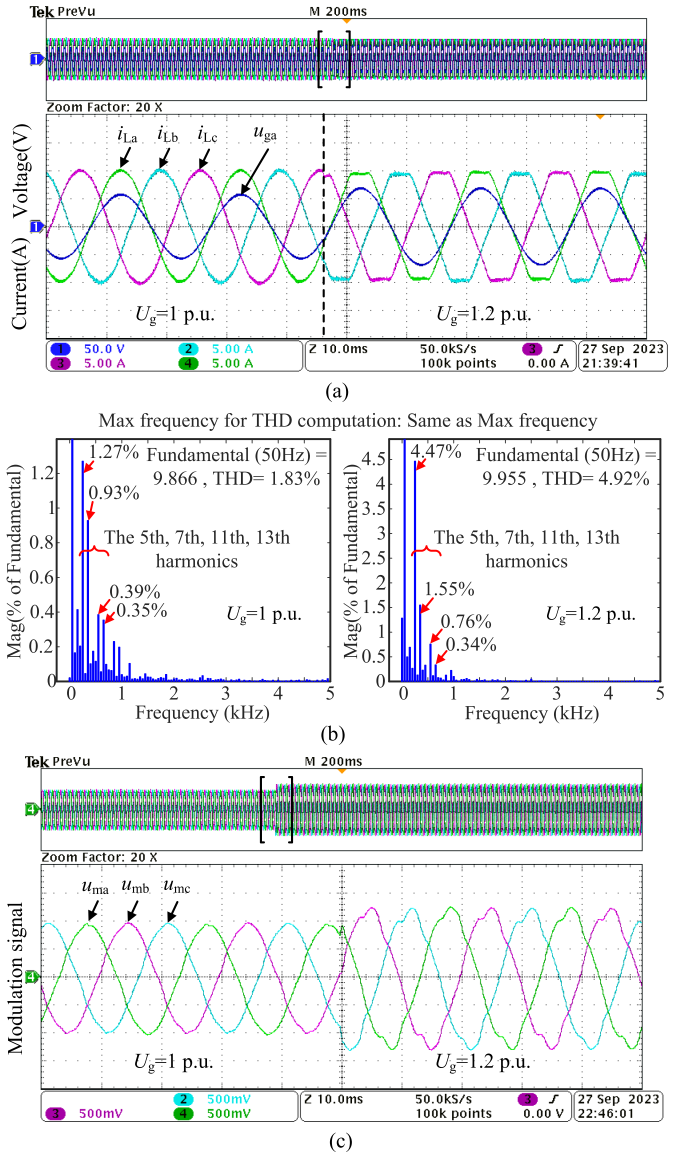

Fig. 22. Experimental waveform of grid voltage swell. (a) Three-phase grid-connected current and grid voltage. (b) Grid-connected current spectrum. (c) Three-phase modulation signal.

experimental results slightly deviate from the previous theoretical and simulation analysis results in terms of oscillation frequency, spectrum, and THD value, because there are a series of non-ideal factors in the experiment, such as the dead-time of the switch transistor, the nonlinear characteristics of the inductor, the nonlinear load characteristics and nonideal output sine of programmable ac source, and experimental device parameter errors.

VI. CONCLUSION

Taking the sustained constant-amplitude oscillation of grid-connected current caused by the increase of k_p and the grid voltage swell as an example, this article analyzes the strong nonlinearity of PWM saturation under these two conditions and introduces the step function to accurately represent it. The accurate stroboscopic mapping model of a grid-connected inverter system considering PWM saturation is established, and it is strictly proved that the expression of the stroboscopic mapping model is the same and unique in different sectors within a fundamental period. Then, the accuracy of the model is verified through numerical simulations in both the time and frequency domains. By using the bifurcation diagram and the root locus of Jacobian matrix, the bifurcation characteristics of the system when PWM saturation occurs under these two operating conditions are analyzed. It is found that under the former working condition, the fixed point of the system becomes unstable, and it is precisely due to the inherent saturation limiting characteristic of PWM that the system undergoes super-critical Hopf bifurcation, forming a stable limit cycle, so the grid-connected current exhibits a sustained constant-amplitude oscillation. In the latter working condition, due to the automatic adjustment effect of closed-loop control, PWM undergoes overmodulation, the content of low-order harmonics in the output voltage u_{ao} and grid-connected current will increase. Due to the low-pass filtering characteristics of the entire closed-loop control system, these low-order harmonics will not be attenuated and will always exist in the system, causing the grid-connected current to exhibit sustained constant-amplitude oscillation, but the fixed point of the system is still stable and does not undergo bifurcation. So far, this article reveals the essential reasons for the oscillation of grid-connected current and its relationship with PWM saturation under these two operating conditions and accurately obtains the boundary of bifurcation parameters. The above-mentioned research findings are confirmed by simulation and experimental results.

APPENDIX A

$$\begin{aligned}
\boldsymbol{PT}_1 = {} & \beta \cdot e^{\boldsymbol{A}(t_1+t_2+t_3+t_4+t_3)}\boldsymbol{G}_1(t_{n2}) \\
& + \boldsymbol{\gamma} \cdot e^{\boldsymbol{A}(t_1+t_2+t_3+t_4+t_3)}\boldsymbol{G}_2(t_{n2}) \\
& - \beta \cdot e^{\boldsymbol{A}(t_1+t_2+t_3+t_4+t_3+t_2)}\boldsymbol{G}_1(t_{n1}) \\
& - \boldsymbol{\gamma} \cdot e^{\boldsymbol{A}(t_1+t_2+t_3+t_4+t_3+t_2)}\boldsymbol{G}_2(t_{n1}) \\
\boldsymbol{PT}_2 = {} & \beta \cdot e^{\boldsymbol{A}(t_1+t_2+t_3+t_4)}\boldsymbol{G}_3(t_{n3}) \\
& + \boldsymbol{\gamma} \cdot e^{\boldsymbol{A}(t_1+t_2+t_3+t_4)}\boldsymbol{G}_4(t_{n3}) \\
& - \beta \cdot e^{\boldsymbol{A}(t_1+t_2+t_3+t_4+t_3)}\boldsymbol{G}_3(t_{n2}) \\
& - \boldsymbol{\gamma} \cdot e^{\boldsymbol{A}(t_1+t_2+t_3+t_4+t_3)}\boldsymbol{G}_4(t_{n2}). \\
\boldsymbol{PT}_3 = {} & \beta \cdot e^{\boldsymbol{A}(t_1+t_2)}\boldsymbol{G}_3(t_{n5}) + \boldsymbol{\gamma} \cdot e^{\boldsymbol{A}(t_1+t_2)}\boldsymbol{G}_4(t_{n5}) \\
& - \beta \cdot e^{\boldsymbol{A}(t_1+t_2+t_3)}\boldsymbol{G}_3(t_{n4}) - \boldsymbol{\gamma} \cdot e^{\boldsymbol{A}(t_1+t_2+t_3)}\boldsymbol{G}_4(t_{n4}) \\
\boldsymbol{PT}_4 = {} & \beta \cdot e^{\boldsymbol{A}t_1}\boldsymbol{G}_1(t_{n6}) + \boldsymbol{\gamma} \cdot e^{\boldsymbol{A}t_1}\boldsymbol{G}_2(t_{n6}) \\
& - \beta \cdot e^{\boldsymbol{A}(t_1+t_2)}\boldsymbol{G}_1(t_{n5}) - \boldsymbol{\gamma} \cdot e^{\boldsymbol{A}(t_1+t_2)}\boldsymbol{G}_2(t_{n5})
\end{aligned} \tag{A1}$$

Note: In different sectors, the expression forms of PT_1, PT_2, PT_3, and PT_4 are same, but the values of $\boldsymbol{G}_1$(t), $\boldsymbol{G}_2$(t), $\boldsymbol{G}_3$(t), $\boldsymbol{G}_4$(t), t_1, t_2, t_3, and t_4 in (A1) are different. Please refer to Appendix B below for specific values.

APPENDIX B

The expressions for $\boldsymbol{G}_1$(t), $\boldsymbol{G}_2$(t), $\boldsymbol{G}_3$(t), and $\boldsymbol{G}_4$(t) in different sectors be expressed as

Sector I:

$$\begin{aligned}
&\boldsymbol{G}_{I1}(t) = \begin{bmatrix} \sin(\omega_o t) \\ \cos(\omega_o t) \end{bmatrix}, \boldsymbol{G}_{I2}(t) = \begin{bmatrix} -\cos(\omega_o t) \\ \sin(\omega_o t) \end{bmatrix}, \\
&\boldsymbol{G}_{I3}(t) = \begin{bmatrix} \sin(\omega_o t - \frac{\pi}{3}) \\ \cos(\omega_o t - \frac{\pi}{3}) \end{bmatrix}, \boldsymbol{G}_{I4}(t) = \begin{bmatrix} -\cos(\omega_o t - \frac{\pi}{3}) \\ \sin(\omega_o t - \frac{\pi}{3}) \end{bmatrix}.
\end{aligned} \tag{A2}$$

Sector II:

$$\begin{aligned}
&\boldsymbol{G}_{\mathrm{II}1}(t) = \begin{bmatrix} -\sin(\omega_o t + \frac{\pi}{3}) \\ -\cos(\omega_o t + \frac{\pi}{3}) \end{bmatrix}, \boldsymbol{G}_{\mathrm{II}2}(t) = \begin{bmatrix} \cos(\omega_o t + \frac{\pi}{3}) \\ -\sin(\omega_o t + \frac{\pi}{3}) \end{bmatrix}, \\
&\boldsymbol{G}_{\mathrm{II}3}(t) = \begin{bmatrix} \sin(\omega_o t - \frac{\pi}{3}) \\ \cos(\omega_o t - \frac{\pi}{3}) \end{bmatrix}, \boldsymbol{G}_{\mathrm{II}4}(t) = \begin{bmatrix} -\cos(\omega_o t - \frac{\pi}{3}) \\ \sin(\omega_o t - \frac{\pi}{3}) \end{bmatrix}.
\end{aligned} \tag{A3}$$

Sector III:

$$\begin{aligned}
&\boldsymbol{G}_{\mathrm{III}1}(t) = \begin{bmatrix} -\sin(\omega_o t + \frac{\pi}{3}) \\ -\cos(\omega_o t + \frac{\pi}{3}) \end{bmatrix}, \boldsymbol{G}_{\mathrm{III}2}(t) = \begin{bmatrix} \cos(\omega_o t + \frac{\pi}{3}) \\ -\sin(\omega_o t + \frac{\pi}{3}) \end{bmatrix}, \\
&\boldsymbol{G}_{\mathrm{III}3}(t) = \begin{bmatrix} -\sin(\omega_o t) \\ -\cos(\omega_o t) \end{bmatrix}, \boldsymbol{G}_{\mathrm{III}4}(t) = \begin{bmatrix} \cos(\omega_o t) \\ -\sin(\omega_o t) \end{bmatrix}.
\end{aligned} \tag{A4}$$

Sector IV:

$$\begin{aligned}
&\boldsymbol{G}_{\mathrm{IV}1}(t) = \begin{bmatrix} -\sin(\omega_o t - \frac{\pi}{3}) \\ -\cos(\omega_o t - \frac{\pi}{3}) \end{bmatrix}, \boldsymbol{G}_{\mathrm{IV}2}(t) = \begin{bmatrix} \cos(\omega_o t - \frac{\pi}{3}) \\ -\sin(\omega_o t - \frac{\pi}{3}) \end{bmatrix}, \\
&\boldsymbol{G}_{\mathrm{IV}3}(t) = \begin{bmatrix} -\sin(\omega_o t) \\ -\cos(\omega_o t) \end{bmatrix}, \boldsymbol{G}_{\mathrm{IV}4}(t) = \begin{bmatrix} \cos(\omega_o t) \\ -\sin(\omega_o t) \end{bmatrix}.
\end{aligned} \tag{A5}$$

Sector V:

$$\begin{aligned}
&\boldsymbol{G}_{\mathrm{V}1}(t) = \begin{bmatrix} -\sin(\omega t - \frac{\pi}{3}) \\ -\cos(\omega t - \frac{\pi}{3}) \end{bmatrix}, \boldsymbol{G}_{\mathrm{V}2}(t) = \begin{bmatrix} \cos(\omega t - \frac{\pi}{3}) \\ -\sin(\omega t - \frac{\pi}{3}) \end{bmatrix}, \\
&\boldsymbol{G}_{\mathrm{V}3}(t) = \begin{bmatrix} \sin(\omega t + \frac{\pi}{3}) \\ \cos(\omega t + \frac{\pi}{3}) \end{bmatrix}, \boldsymbol{G}_{\mathrm{V}4}(t) = \begin{bmatrix} -\cos(\omega t + \frac{\pi}{3}) \\ \sin(\omega t + \frac{\pi}{3}) \end{bmatrix}.
\end{aligned} \tag{A6}$$

Sector VI:

$$\begin{aligned}
&\boldsymbol{G}_{\mathrm{VI}1}(t) = \begin{bmatrix} \sin(\omega_o t) \\ \cos(\omega_o t) \end{bmatrix}, \boldsymbol{G}_{\mathrm{VI}2}(t) = \begin{bmatrix} -\cos(\omega_o t) \\ \sin(\omega_o t) \end{bmatrix}, \\
&\boldsymbol{G}_{\mathrm{VI}3}(t) = \begin{bmatrix} \sin(\omega_o t + \frac{\pi}{3}) \\ \cos(\omega_o t + \frac{\pi}{3}) \end{bmatrix}, \boldsymbol{G}_{\mathrm{VI}4}(t) = \begin{bmatrix} -\cos(\omega_o t + \frac{\pi}{3}) \\ \sin(\omega_o t + \frac{\pi}{3}) \end{bmatrix}.
\end{aligned} \tag{A7}$$

The expressions for t_1, t_2, t_3, t_4 in different sectors and $t_{\mathrm{n}1}$, $t_{\mathrm{n}2}$, $t_{\mathrm{n}3}$, $t_{\mathrm{n}4}$ be expressed as

$$\text{(I)}\begin{cases} t_1 = \frac{1}{2}[1 - d_a(n)] \cdot T_s \\ t_2 = \frac{1}{2}[d_a(n) - d_b(n)] \cdot T_s \\ t_3 = \frac{1}{2}[d_b(n) - d_c(n)] \cdot T_s \\ t_4 = d_c(n) \cdot T_s \end{cases}$$

$$\text{(II)}\begin{cases} t_1 = \frac{1}{2}[1 - d_b(n)] \cdot T_s \\ t_2 = \frac{1}{2}[d_b(n) - d_a(n)] \cdot T_s \\ t_3 = \frac{1}{2}[d_a(n) - d_c(n)] \cdot T_s \\ t_4 = d_c(n) \cdot T_s \end{cases} \tag{A8}$$

$$\text{(III)}\begin{cases} t_1 = \frac{1}{2}[1 - d_b(n)] \cdot T_s \\ t_2 = \frac{1}{2}[d_b(n) - d_c(n)] \cdot T_s \\ t_3 = \frac{1}{2}[d_c(n) - d_a(n)] \cdot T_s \\ t_4 = d_a(n) \cdot T_s \end{cases}$$

$$\text{(IV)}\begin{cases} t_1 = \frac{1}{2}[1 - d_c(n)] \cdot T_s \\ t_2 = \frac{1}{2}[d_c(n) - d_b(n)] \cdot T_s \\ t_3 = \frac{1}{2}[d_b(n) - d_a(n)] \cdot T_s \\ t_4 = d_a(n) \cdot T_s \end{cases} \tag{A9}$$

$$\text{(V)}\begin{cases} t_1 = \frac{1}{2}[1 - d_c(n)] \cdot T_s \\ t_2 = \frac{1}{2}[d_c(n) - d_a(n)] \cdot T_s \\ t_3 = \frac{1}{2}[d_a(n) - d_b(n)] \cdot T_s \\ t_4 = d_b(n) \cdot T_s \end{cases}$$

$$\text{(VI)}\begin{cases} t_1 = \frac{1}{2}[1 - d_a(n)] \cdot T_s \\ t_2 = \frac{1}{2}[d_a(n) - d_c(n)] \cdot T_s \\ t_3 = \frac{1}{2}[d_c(n) - d_b(n)] \cdot T_s \\ t_4 = d_b(n) \cdot T_s \end{cases} \tag{A10}$$

$$\begin{cases} t_n = nT_s \\ t_{n1} = nT_s + t_1 \\ t_{n2} = nT_s + t_1 + t_2 \\ t_{n3} = nT_s + t_1 + t_2 + t_3 \\ t_{n4} = nT_s + t_1 + t_2 + t_3 + t_4 \\ t_{n5} = nT_s + t_1 + t_2 + t_3 + t_4 + t_3 \\ t_{n6} = nT_s + t_1 + t_2 + t_3 + t_4 + t_3 + t_2 \\ t_{n+1} = (T_s + nT_s) \end{cases} . \tag{A11}$$

APPENDIX C

The Jacobian matrix is derived as

$$\boldsymbol{J} = \begin{bmatrix} \sigma(1,1) & \sigma(1,2) & 0 & 0 & \frac{\partial F_1}{\partial d_a} & \frac{\partial F_1}{\partial d_b} & \frac{\partial F_1}{\partial d_c} \\ \sigma(2,1) & \sigma(2,2) & 0 & 0 & \frac{\partial F_2}{\partial d_a} & \frac{\partial F_2}{\partial d_b} & \frac{\partial F_2}{\partial d_c} \\ -k_i T_s & 0 & 1 & 0 & 0 & 0 & 0 \\ 0 & -k_i T_s & 0 & 1 & 0 & 0 & 0 \\ \frac{\partial F_5}{\partial i_{Ld}} & \frac{\partial F_5}{\partial i_{Lq}} & \frac{\partial F_5}{\partial u_{\text{icond}}} & \frac{\partial F_5}{\partial u_{\text{iconq}}} & 0 & 0 & 0 \\ \frac{\partial F_6}{\partial i_{Ld}} & \frac{\partial F_6}{\partial i_{Lq}} & \frac{\partial F_6}{\partial u_{\text{icond}}} & \frac{\partial F_6}{\partial u_{\text{iconq}}} & 0 & 0 & 0 \\ \frac{\partial F_7}{\partial i_{Ld}} & \frac{\partial F_7}{\partial i_{Lq}} & \frac{\partial F_7}{\partial u_{\text{icond}}} & \frac{\partial F_7}{\partial u_{\text{iconq}}} & 0 & 0 & 0 \end{bmatrix}_{\boldsymbol{x}'=\boldsymbol{x}'_0} \tag{A12}$$

where

$$\frac{\partial F_1}{\partial d_a} = \frac{R_f T_s}{2L_f} ch\left(\frac{R_f T_s}{2L_f} d_a\right) \Lambda_1^n(1,1)$$

$$\frac{\partial F_1}{\partial d_b} = \frac{R_f T_s}{2L_f} ch\left(\frac{R_f T_s}{2L_f} d_b\right) [\Lambda_2^n(1,1) - \Lambda_1^n(1,1)]$$

$$\frac{\partial F_1}{\partial d_c} = -\frac{R_f T_s}{2L_f} ch\left(\frac{R_f T_s}{2L_f} d_c\right) \Lambda_2^n(1,1)$$

$$\frac{\partial F_2}{\partial d_a} = \frac{R_f T_s}{2L_f} ch\left(\frac{R_f T_s}{2L_f} d_a\right) \Lambda_1^n(2,1)$$

$$\frac{\partial F_2}{\partial d_b} = \frac{R_f T_s}{2L_f} ch\left(\frac{R_f T_s}{2L_f} d_b\right) [\Lambda_2^n(2,1) - \Lambda_1^n(2,1)]$$

$$\frac{\partial F_2}{\partial d_c} = -\frac{R_f T_s}{2L_f} ch\left(\frac{R_f T_s}{2L_f} d_c\right) \Lambda_2^n(2,1)$$

$$\frac{\partial F_5}{\partial i_{Ld}} = \sqrt{\frac{2}{3}} \frac{1}{U_{dc}} [-\cos(\omega_o n T_s) k_p - \sin(\omega_o n T_s) \omega_o L_f]$$

$$\frac{\partial F_5}{\partial i_{Lq}} = \sqrt{\frac{2}{3}} \frac{1}{U_{dc}} [-\cos(\omega_o n T_s) \omega_o L_f + \sin(\omega_o n T_s) k_p]$$

$$\frac{\partial F_5}{\partial u_{\text{icond}}} = \sqrt{\frac{2}{3}} \frac{1}{U_{dc}} \cos(\omega_o n T_s)$$

$$\frac{\partial F_5}{\partial u_{\text{iconq}}} = -\sqrt{\frac{2}{3}} \frac{1}{U_{dc}} \sin(\omega_o n T_s)$$

$$\frac{\partial F_6}{\partial i_{Ld}} = \sqrt{\frac{2}{3}} \frac{1}{U_{dc}} \left[-\cos\left(\omega_o n T_s - \frac{2\pi}{3}\right) k_p - \sin\left(\omega_o n T_s - \frac{2\pi}{3}\right) \omega_o L_f\right]$$

$$\frac{\partial F_6}{\partial i_{Lq}} = \sqrt{\frac{2}{3}} \frac{1}{U_{dc}} \left[-\cos\left(\omega_o n T_s - \frac{2\pi}{3}\right) \omega_o L_f + \sin\left(\omega_o n T_s - \frac{2\pi}{3}\right) k_p\right]$$

$$\frac{\partial F_6}{\partial u_{\text{icond}}} = \sqrt{\frac{2}{3}} \frac{1}{U_{dc}} \cos\left(\omega_o n T_s - \frac{2\pi}{3}\right)$$

$$\frac{\partial F_6}{\partial u_{\text{iconq}}} = -\sqrt{\frac{2}{3}} \frac{1}{U_{dc}} \sin\left(\omega_o n T_s - \frac{2\pi}{3}\right)$$

$$\frac{\partial F_7}{\partial i_{Ld}} = \sqrt{\frac{2}{3}}\frac{1}{U_{dc}}\left[-\cos\left(\omega_o nT_s + \frac{2\pi}{3}\right)k_p - \sin\left(\omega_o nT_s + \frac{2\pi}{3}\right)\omega_o L_f\right]$$

$$\frac{\partial F_7}{\partial i_{Lq}} = \sqrt{\frac{2}{3}}\frac{1}{U_{dc}}\left[-\cos\left(\omega_o nT_s + \frac{2\pi}{3}\right)\omega_o L_f + \sin\left(\omega_o nT_s + \frac{2\pi}{3}\right)k_p\right]$$

$$\frac{\partial F_7}{\partial u_{\text{icond}}} = \sqrt{\frac{2}{3}}\frac{1}{U_{dc}}\cos\left(\omega_o nT_s + \frac{2\pi}{3}\right)$$

$$\frac{\partial F_7}{\partial u_{\text{iconq}}} = -\sqrt{\frac{2}{3}}\frac{1}{U_{dc}}\sin\left(\omega_o nT_s + \frac{2\pi}{3}\right).$$

REFERENCES

[1] B. Kroposki et al., "Achieving a 100% renewable grid: Operating electric power systems with extremely high levels of variable renewable energy," *IEEE Power Energy Mag.*, vol. 15, no. 2, pp. 61–73, Mar./Apr. 2017.

[2] J. M. Carrasco et al., "Power-electronic systems for the grid integration of renewable energy sources: A survey," *IEEE Trans. Ind. Electron.*, vol. 53, no. 4, pp. 1002–1016, Jun. 2006.

[3] Q. Liu, T. Caldognetto, and S. Buso, "Review and comparison of grid-tied inverter controllers in microgrids," *IEEE Trans. Power Electron.*, vol. 35, no. 7, pp. 7624–7639, Jul. 2020.

[4] F. Blaabjerg, R. Teodorescu, M. Liserre, and A. V. Timbus, "Overview of control and grid synchronization for distributed power generation systems," *IEEE Trans. Ind. Electron.*, vol. 53, no. 5, pp. 1398–1409, Oct. 2006.

[5] H. Ashara and T. Kousaka, "Bifurcation analysis in a PWM current-controlled H-bridge inverter," *Int. J. Bifurcation Chaos*, vol. 21, no. 3, pp. 985–996, Oct. 2011.

[6] Y. Han, X. Fang, and P. Yang, C. Wang, L. Xu, and J. M. Guerrero, "Stability analysis of digital-controlled single-phase inverter with synchronous reference frame voltage control," *IEEE Trans. Power Electron.*, vol. 33, no. 7, pp. 6333–6350, Jul. 2018.

[7] T. H. Wu et al., "Quantitative analysis of sustained oscillation associated with saturation non-linearity in a grid-connected voltage source converter," *IET Renewable Power Gener.*, vol. 15, no. 4, pp. 865–876, Sep. 2020.

[8] Q. Peng, Q. Jiang, Y. Yang, T. Liu, H. Wang, and F. Blaabjerg, "On the stability of power electronics-dominated systems: Challenges and potential solutions," *IEEE Trans. Ind. Appl.*, vol. 55, no. 6, pp. 7657–7670, Dec. 2019.

[9] G. Revel et al., "Multi-parameter bifurcation analysis of subsynchronous interactions in DFIG-based wind farms," *Electric Power Syst. Res.*, vol. 55, no. 6, pp. 643–652, Nov. 2016.

[10] L. P. Kun, C. P. Bikash, and R. Gupta, and K. J. Dyke, "Stability analysis of a PMSG-based large offshore wind farm connected to a VSC-HVDC," *IEEE Trans. Energy Convers.*, vol. 32, no. 3, pp. 1166–1176, Sep. 2017.

[11] Z. Xie, X. Zhang, X. Zhang, S. Yang, and L. Wang, "Improved ride-through control of DFIG during grid voltage swell," *IEEE Trans. Ind. Electron.*, vol. 62, no. 6, pp. 3584–3594, Jun. 2015.

[12] M. K. Mishra and V. N. Lal, "An enhanced control strategy to mitigate grid current harmonics and power ripples of grid-tied PV system without PLL under distorted grid voltages," *IEEE J. Emerg. Sel. Topics Power Electron.*, vol. 10, no. 4, pp. 4587–4602, Aug. 2022.

[13] O. R. Fendrich, "Describing functions and limit cycles," *IEEE Trans. Autom. Control*, vol. 37, no. 4, pp. 486–487, Apr. 1992.

[14] X. H. Wang et al., "Impact of controller saturation on instability behavior of grid-connected inverters," *IEEE Trans. Power Electron.*, vol. 37, no. 7, pp. 7739–7750, Jul. 2022.

[15] S. Shah et al., "Impedance-based prediction of distortions generated by resonance in grid-connected converters," *IEEE Trans. Sustain. Energy*, vol. 34, no. 3, pp. 1264–1275, Sep. 2019.

[16] S. Shah et al., "Large-signal impedance-based modeling and mitigation of resonance of converter-grid systems," *IEEE Trans. Sustain. Energy*, vol. 10, no. 3, pp. 1439–1449, Jul. 2019.

[17] J. Sun, "Small-signal methods for AC distributed power systems–a review," *IEEE Trans. Power Electron.*, vol. 24, no. 11, pp. 2545–2554, Nov. 2009.

[18] A. Gelb and W. E. V. Velde, *Multiple-Input Describing Functions and Nonlinear System Design*. New York, NY, USA: McGraw-Hill, 1968.

[19] S. Banerjee, P. Ranjan, and C. Grebogi, "Bifurcations in two-dimensional piecewise smooth maps-theory and applications in switching circuits," *IEEE Trans. Circuits Syst. I, Fundam. Theory Appl.*, vol. 47, no. 5, pp. 633–643, May 2000.

[20] S. Kapat, S. Banerjee, and A. Patra, "Discontinuous map analysis of a dc-dc converter governed by pulse skipping modulation," *IEEE Trans. Circuits Syst. I, Regular Papers*, vol. 57, no. 7, pp. 1793–1801, Jul. 2010.

[21] M. Li, D. Dai, and X. K. Ma, "Slow-scale and fast-scale Instabilities in voltage-mode controlled full-bridge inverter," *Circuits Syst., Signal Proc.*, vol. 27, no. 27, pp. 811–831, Jul. 2008.

[22] H. B. Cao, F. Q. Wang, and J. J. Liu, "Analysis of fast-scale instability in three-level T-type single-phase inverter feeding diode-bridge rectifier with inductive load," *IEEE Trans. Power Electron.*, vol. 37, no. 12, pp. 15066–15083, Dec. 2022.

[23] B. Lei et al., "Bifurcation analysis in a digital-controlled H-bridge grid-connected inverter," *Int. J. Bifurcation Chaos*, vol. 24, no. 1, pp. 0021–00215, Nov. 2014.

[24] X. L. Wu, G. C. Xiao, and B. Lei, "Simplified discrete-time modeling for convenient stability prediction and digital control design," *IEEE Trans. Power Electron*, vol. 28, no. 11, pp. 5333–5342, Nov. 2013.

[25] B. Lei, G. C. Xiao, and X. L. Wu, "Analysis of partial oscillation phenomenon in a digital-controlled three-phase inverter," *Acta Physica Sinica*, vol. 62, no. 4, pp. 5021–50211, Nov. 2013.

[26] T. H. Wu et al., "Impedance modelling of grid-connected voltage-source converters considering the saturation nonlinearity," *IET Gener., Transmiss. Distrib.*, vol. 14, no. 21, pp. 4815–4823, Sep. 2020.

[27] C. K. Tse, *Complex Behavior of Switching Power Converters*, 1st ed. Boca Raton, FL, USA: CRC Press, 2004.

[28] M. Lu, X. Wang, P. C. Loh, and F. Blaabjerg, "Graphical evaluation of time-delay compensation techniques for digitally-controlled converters," *IEEE Trans. Power Electron.*, vol. 33, no. 3, pp. 2601–2614, Mar. 2018.

[29] K. L. Zhou and D. W. Wang, "Relationship between space-vector modulation and three phase carrier-based PWM: A comprehensive analysis," *IEEE Trans. Ind. Electron.*, vol. 49, no. 1, pp. 186–196, Feb. 2002.

Le Chen (Student Member, IEEE) received the B.S. degree in electrical engineering from Shaanxi University of Science and Technology, Xi'an, China, in 2016, and the M.S. degree in electrical engineering from East China Jiaotong University, Nanchang, China, in 2020. He is currently working toward the Ph.D. degree in electrical engineering with Xi'an Jiaotong University, Xi'an, China.

His research interests include modeling, control, and stability analysis of power electronic systems.

Yingjie He (Senior Member, IEEE) received the B.S., M.S., and Ph.D. degrees from Huazhong University of Science and Technology, Wuhan, China, in 1999, 2003, and 2007, respectively.

He was then with the Power Electronics and Renewable Energy Center, Xi'an Jiaotong University (XJTU), Xi'an, China, as a Postdoctoral Researcher, and with Aalborg University, Aalborg, Denmark, as a Visiting Scholar. He is currently an Associate Professor and Doctoral Supervisor with XJTU. He is selected as the High-level Talent of Shaanxi Power Supply Society and the High-level Talent of Zhenjiang, Jiangsu, China. He is also the Executive Director of IEEE Flexible AC Transmission Technology Subcommittee (China), Executive Director of Shaanxi Power Supply Society, Senior Member of China Electrotechnical Society, Member of Power Quality Special Committee of China Power Supply Society, and appraisal expert of National Natural Science Foundation and Ministry of Science and Technology of China. He has authored or coauthored more than 100 journal and conference papers such as IEEE TRANSACTIONS ON POWER ELECTRONICS and IEEE TRANSACTIONS ON INDUSTRIAL ELECTRONICS. His research interests include multilevel converter and its control technology, application of power electronics in power system, power quality and its control technology.

He was the recipient of the Second Prize of Science and Technology Progress from China Power Supply Society in 2021, the Science and Technology Progress Award from Shaanxi Power Supply Society in 2022, and the Special Contribution Award from Proceedings of the CSEE.

Yixiao Zhu received the B.S. degree in electrical engineering from South China University of Technology, Guangzhou, China, in 2019, and the M.S. degree in electrical engineering from Xi'an Jiaotong University, Xi'an, China, in 2020.

His main research interests include power springs and power quality control technology.

Jinjun Liu (Fellow, IEEE) received the B.S. and Ph.D. degrees in electrical engineering from Xi'an Jiaotong University (XJTU), Xi'an, China, in 1992 and 1997, respectively.

He then joined the XJTU Electrical Engineering School as a Faculty. From 1999 to 2002, he was with the Center for Power Electronics Systems, Virginia Polytechnic Institute and State University, Blacksburg, VA, USA, as a Visiting Scholar. In late 2002, he was promoted to a Full Professor and then the Head of the Power Electronics and Renewable Energy Center at XJTU, which now comprises 21 faculty members and over 150 graduate students and carries one of the leading power electronics programs in China. From 2005 to 2010, he served as an Associate Dean of Electrical Engineering School, XJTU, and from 2009 to 2015, the Dean for Undergraduate Education of XJTU. He is currently a XJTU Distinguished Professor of Power Electronics. He has coauthored three books (including one textbook), authored or coauthored more than 500 technical papers in peer-reviewed journals and conference proceedings, holds more than 50 invention patents (China/US/Europe), and delivered for many times plenary keynote speeches and tutorials at IEEE conferences or China national conferences in power electronics area. His research interests include modeling, control, and design methods for power converters and electronified power systems, power quality control and utility applications of power electronics, and micro-grids for sustainable energy and distributed generation.

Dr. Liu was the recipient of eight times governmental awards at national level or provincial/ministerial level for scientific research/teaching achievements. He was also the recipient of the 2006 Delta Scholar Award, the 2014 Chang Jiang Scholar Award, the 2014 Outstanding Sci-Tech Worker of the Nation Award, the 2016 State Council Special Subsidy Award, and IEEE TRANSACTIONS ON POWER ELECTRONICS 2016 and 2021 Prize Paper Award. He served as the IEEE Power Electronics Society Region 10 Liaison and then China Liaison for 10 years, an Associate Editor for IEEE TRANSACTIONS ON POWER ELECTRONICS for 13 years, 2015–2019 Executive Vice President and 2020–2021 Vice President for membership of IEEE PELS. He is on the Board of China Electrotechnical Society and was elected the Vice President in 2013 and the Secretary General in 2018 of the CES Power Electronics Society. Since 2013, he has been the Vice President for International Affairs, China Power Supply Society (CPSS) and since 2016, the inaugural Editor-in-Chief of *CPSS Transactions on Power Electronics and Applications*. Since 2013, he has been serving as the Vice Chair of the Chinese National Steering Committee for College Electric Power Engineering Programs.